J. Appl. Comput. Mech., xx(x) (2026) 1-19
DOI: 10.22055/jacm.2026.48643.5388

ISSN: 2383-4536
jacm.scu.ac.ir

Shahid Chamran University of Ahvaz

Journal of Applied and Computational Mechanics

Research Paper

Magneto-Convection Flow of Micropolar Eyring-Powell Fluid from a Revolving Cone with Hall Current and Ohmic Heating Effects

Shaik Abdul Gaffar[1], Osman Anwar Bég[2], Tasveer A. Beg[3], Sireetorn Kuharat[2], Pedakamu Ramesh Reddy[4]

[1] Supporting Requirements Department, Sciences and Mathematics Unit, University of Technology and Applied Sciences Salalah, 211, Sultanate of Oman, Email: AbdulGaffar.Shaik@utas.edu.om

[2] Multi-Physical Engineering Sciences Group, Mechanical Engineering Department, Corrosion and Coatings Lab, Room 3-08, SEE Building, University of Salford, Manchester, M54WT, United Kingdom, Email: O.A.Beg@salford.ac.uk (O.A.B.); S.Kuharat2@salford.ac.uk (S.K.)

[3] Engineering Mechanics Research, Israfil House, Dickenson Rd., Manchester, M13, United Kingdom, Email: tasveerabeg@gmail.com

[4] Department of Mathematics, Madanapalle Institute of Technology & Sciences, Madanapalle, 517325, India, Email: prreddy.mits@gmail.com

Received July 28 2025; Revised February 07 2026; Accepted for publication February 11 2026.
✉ Corresponding author: S. Abdul Gaffar (AbdulGaffar.Shaik@utas.edu.om)

Abstract. As a simulation of electromagnetic rheological spin coating flow, a theoretical study is conducted on the nonlinear, steady-state boundary layer flow and heat transfer of an incompressible Eyring-Powell non-Newtonian micropolar fluid about a spinning cone with magnetic field, Hall current, viscous dissipation, Ohmic (Joule) heating and power-law variation in temperature. In order to simulate the polymer microstructural and shearing features, the Eringen's micropolar and Eyring-Powell rheological models are coupled. The micropolar model accurately simulates certain polymeric fluids and includes micro-element gyratory rotating motions. The transformed conservation equations are solved numerically subject to physically appropriate boundary conditions using a second order accurately implicit finite-difference Keller Box technique. Verification with previous special cases from the literature is included. The novelty of the present study is therefore the simultaneous consideration of viscous dissipation, Joule magnetic heating, Hall current and the combined Eyring–Powell micropolar non-Newtonian model for spin coating on a non-isothermal rotating cone. The influence of a number of emerging non-dimensional parameters, namely first and second Eyring-Powell rheological fluid parameters (ε, δ), surface temperature exponent (m), Prandtl number (Pr), magnetic interaction parameter (M), Hall current parameter (β_e), Eckert number (Ec), micropolar fluid material parameters (V_1, λ), Eringen vortex viscosity parameter (K) and dimensionless tangential coordinate (ξ) on axial and tangential velocities, angular velocity and temperature evolution in the boundary layer regime are examined in detail. Furthermore, the effects of these parameters on Nusselt number (wall heat transfer rate), wall couple stress and both axial and tangential skin friction are also investigated. Increasing ε induces a weak axial flow near the cone surface, followed by a pronounced deceleration beyond a critical distance that persists into the freestream. In contrast, the tangential velocity is strongly enhanced throughout the boundary layer regime with increasing ε. Micro-element angular velocity increases away from the wall, though its magnitude remains smaller than near the cone surface. Additionally, higher values of ε significantly elevate the temperature and thicken the thermal boundary layer. Increasing K causes strong axial flow deceleration away from the cone surface, while the tangential velocity is enhanced. Higher values of K also lead to a significant rise in temperature across the boundary layer. Furthermore, increasing m results in pronounced axial deceleration, attenuation of micro-rotation and a substantial reduction in temperature. An increase in M, induces deceleration in both axial and tangential velocities, while significantly enhancing micro-rotation, particularly away from the cone surface. Temperature is also markedly elevated throughout the boundary layer with increasing M. Furthermore, increasing Ec, accounting for viscous and Joule heating effects, enhances the axial velocity, temperature, and micro-rotation, while suppressing the tangential velocity.

Keywords: Eyring-powell micropolar fluid; Hall current; Magnetohydrodynamics (MHD); Ohmic and viscous heating; Revolving cone; Spin coating.

1. Introduction

Non-Newtonian fluid dynamics continues to attract attention in engineering sciences owing to ever increasing applications in industrial polymer coating systems [1]. The nature of non-Newtonian (rheological) liquids varies considerably depending on the molecular weight and loading conditions. Many different constitutive formulations have been developed over decades to simulate the diverse variety of phenomena encountered including shear thinning/thickening, viscoelasticity, viscoplasticity (yield stress

Published online: February 23 2026

behavior), stress relaxation and retardation etc. [2]. This approach is continuum-based as opposed to molecular dynamics [3]. Many excellent rheological models have been deployed in coating fluid dynamics simulations in recent years. These include the Casson viscoplastic model, Herchel-Bulkley power-law/yield stress model, Carreau pseudoplastic model, Oldroyd-B viscoelastic model, Cross model, Sisko model, Maxwell UCM model and others. All these models provide various levels of accuracy in analyzing for example high-molecular weight polymers or "macromolecules'' in the form of polymer solutions or polymer melts in coating deposition technologies [4]. Ali et al. [5] used finite difference and variational finite element methods to compute the axisymmetric coating boundary layer flow of wire geometries with Giesekus viscoelastic fluid. Bajaj et al. [6] examined the slot coating flow of viscoelastic dilute polymer solutions using the Oldroyd-B and FENE-P models and a finite element method with elliptic domain mapping for the unknown free surface. They noted that for the case of dilute polymer solutions, with increment in Weissenberg number, there is a displacement in the stagnation point on the free surface moves towards the static contact line and contraction in the recirculation zone. They further showed that for ultra-dilute solutions, complexities arise due to high gradients in the boundary layers at the free surface. Norouzi et al. [7] computed the thermal convection in FENE-P viscoelastic fluids in isothermal conduits. Zafar et al. [8] investigated the Maxwell viscoelastic polymer roll coating over a porous web using the lubrication approximation theory, which provides an alternative to another popular model known as the Eyring-Powell model [9]. Hayat et al. [10] investigated the Cattaneo-Christov heat flux model of Oldroyd-B fluid across a non-linear stretching surface with varying thickness using a homotopic technique. Sharma and Sachin [11] analyzed the MHD flow of non-Newtonian fluid over a stretching sheet, incorporating nonlinear thermal radiation and viscous dissipation.

An alternative non-Newtonian model is the Eyring-Powell (E-P) three-parameter model [9] which exhibits a fluid time scale which is very sensitive to variations in the zero-shear rate viscosity but mildly sensitive to the variations in the infinite shear rate viscosity. Hassan et al. [12] conducted a second law thermodynamic analysis on Eyring-Powell thermal boundary layer flows. Rosca and Pop [13] computed the thermal convective boundary layer flow E-P fluid over a porous wall in a parallel free stream when the surface is moving into the origin (shrinking surface). They used the MATLAB function bvp4c and computed dual solutions are found for negative values of the moving surface parameter, although they did not give any tangible physical interpretation of the non-Newtonian effects. Jalil et al. [14] studied the thermal convection in boundary layer coating flow of an E-P fluid over stretching surface. Aatif et al. [15] simulated numerically the non-Fourier heat flux effects in boundary layer convection flow of an E-P polymer from a moving porous surface. They utilized the 5th order Runge–Kutta method (R-K5) in MATLAB with a three-stage Lobatto IIIA algorithm in MATLAB and observed that flow acceleration is induced with greater Eyring-Powell first parameter whereas it is reduced with Eyring-Powell second parameter. They further noted that strong wall suction retards the coating rate and increases momentum boundary layer thickness. Iman and Waleed [16] reported the Powell-Eyring fluid flow induced by a stretching surface with various thermos-physical characteristics. Numerical Shooting approach was integrated to address the governing equations for the specified problems. Zahra et al. [17] discussed the effects of MHD, Joule heating and thermal radiation on Eyring-Powell fluid flow past a nonlinear variably thicken stretching surface using RK-5 technique.

In recent years a new sub-group of multi-functional magnetic polymers [18] has emerged. These contain embedded magnetic particles which respond to external electromagnetic fields. These complex magnetically controllable colloids exhibit rheological properties which can be finely tuned on the nano- or micro-scale. They are also known as electro-conductive polymers (ECPs) and magnetoelectric polymers (MEPs) and effectively combine the characteristics of conventional polymers with magnetohydrodynamic (MHD) or electrically conducting liquids [19]. By suspending metallic conducting particles in polymers, the electro-active phases of the coating material can be engineered to specific needs under the action of an external magnetic field. The binding can be either chemical or physical and pre-crosslinked supra-colloidal magnetic polymers (SMPs) can be synthesized with both magnetic and Van-der-Waals-type forces. These developments have stimulated considerable interest in magneto-rheological polymer fluid dynamics simulation including smart coating transport phenomena simulation. Kumaran et al. [20] deployed a finite difference scheme to compute the magnetized thermal coating of reactive E-P rheological nanofluid flow over a cylindrical geometry with variable thermal conductivity variation and radiative heat flux effects on chemically reacting. They noted that both momentum and boundary layer thicknesses are strongly influenced by E-P rheological parameters, and that nanoparticle concentration is reduced with higher E-P parameter, first-order chemical reaction and Brownian dynamic parameter magnitudes. Khan [21] studied the hydromagnetic viscoelastic Eyring–Powell fluid wire coating flow with temperature-dependent viscosity and a Runge–Kutta 4th-order method and semi-numerical technique homotopy analysis method (HAM). Narayana et al. [22] examined the magnetohydrodynamic E-P convective flow from a linearly stretching sheet, noting that the first and second E-P non-Newtonian material parameters exert opposite effects on momentum and heat transfer characteristics. Further investigations deploying the E-P model in magnetized boundary layer polymeric coating flows include Parmar and Jain [23] (who considered a porous cylinder) and Najeeb et al. [24] (who studied a vertical stretching sheet regime with thermophoresis and chemical reaction effects).

As noted earlier [18, 19] many novel electroconductive polymers feature embedded particles to achieve optimized performance. This modifies the micro-rheology of the resulting materials and conventional non-Newtonian models are insufficient for simulating the characteristics of the micro-elements. Embedded particles can rotate, which also influences viscosity. To simulate angular momentum of suspended particles, Eringen [25] introduced the micropolar fluid model in which gyratory (rotational) degrees of freedom are present for the rigid, non-deformable particles, in addition to the standard linear degrees of freedom in Navier-Stokes classical viscous model. Micropolar fluids are a simpler version of the more general micromorphic fluid in which the particles cannot deform i.e., axially contract or extend. It is therefore a generalization of the simpler Navier-Stokes viscous model wherein extra angular momentum balance (micro-rotation) equations which feature the additional degrees of freedom (via a gyration vector) are included. The equations governing the flow of micropolar fluids therefore involve a spin vector and a microinertia tensor in addition to the customary velocity vector featuring in the linear momentum-based Newtonian (Navier-Stokes) model. Micropolar fluids can support body couples, couple stresses, and a non-symmetric stress tensor. In micropolar fluids, the macroscopic velocity field is coupled with the particle rotational motion, and vortex viscosity acts as a coupling constant. The Navier-Stokes model is therefore a special case of Eringen's micropolar fluid model corresponding to the scenario when micro-rotation effects (angular momentum) vanish [26]. Micropolar theory has been successfully deployed in numerous coating fluid dynamics applications including blade coating [27], substrate reactive non-Newtonian polymer coating flows [28], contact mechanics in tribology [29] and thermal film layer deposition on curved bodies. These investigations all confirmed the significant modification in velocity and temperature distributions produced with micropolar rheological effects. Abhishek and Ram [30] examined the shear-rate optimization in unsteady stagnation-point flow of a micropolar ternary nanofluid over a stationary plate using statistical analysis.

The above non-Newtonian coating flow studies have neglected rotation of the substrate. Spin coating is a special manufacturing technique in which engineering components can be more homogenously coated on a curved rotating body e.g., sphere, cone, cylinder, ellipse, etc. It is popular in the aerospace, civil, marine and micro-electronics industries. Spin coating generally involves four key stages- deposition, substrate spin up/acceleration, constant rotation rate stage (the fluid viscosity controls fluid thinning) and continuous rotating rate stage (in which evaporation of the solvent continues to dominate the thinning behavior of the spin coating liquid). The centrifugal forces produced by the spinning substrate body undergoing coating can be manipulated to achieve modifications in the consistency of the surface finishing. The rotating spreading coating constitutes an incompressible external boundary layer regime which may be steady or unsteady depending on the rate of rotation [31]. Many engineers and applied mathematicians have investigated rotational coating flows on different geometrical configurations and with a variety of non-Newtonian models. Recent studies include Patil and Benwadi [32] (Williamson nanofluids), Kumar and Sahu [33] (rotating elliptic cylindrical ducts), Weidner [34] (thin films on hyperbolic paraboloidal substrates), Lee et al. [35] (slender shells), Kang et al. [36] (rotating spherical bodies) and Wang [37] (spinning cones and discs). Oke and Mutuku [38] studied the boundary layer flow of E-P fluid over the rotating upper horizontal surface of a paraboloid of revolution. They used a shooting technique with the Runge-Kutta-Gill method, noting that at low Coriolis force, temperature values (and thermal boundary layer thickness) are boosted with Eyring-Powell parameter whereas at high Coriolis force, they are depleted. Mustafa [39] investigated non-Fourier heat flux effects on external boundary layer flow on a rotating stretching surface. Ibrahim [40] computed the three-dimensional boundary layer flow of a Powell-Eyring nanofluid from a rotating surface. Nadeem and Saleem [41] studied the time-dependent boundary layer thermal solutal flow of a rotating Eyring–Powell fluid from a spinning cone using the optimal homotopy analysis method.

The objective of the present study is to investigate a range of multi-physical effects on laminar magnetohydrodynamic (MHD) convection boundary layer flow and heat transfer of Eyring –Powell micropolar non-Newtonian coating fluid from a revolving cone with power-law variation in surface temperature. Microstructural features of magnetic polymers have been shown to be critical to their optimized performance [42]. Micropolar fluid models have been shown to capture such phenomena quite accurately. In addition, viscous heating [43, 44] is included in the model since magnetic polymers are known to exhibit this phenomenon (internal friction) even at low speeds. Furthermore, Ohmic heating (Joule magnetic dissipation) [45, 46] is also featured and involves the resistance to flow generated by magnetic fields, a prominent characteristic in modern electroconductive polymers. Finally, Hall current effects are incorporated which feature in various magnetic coating processes involving polymers [47, 48]. The model provides the basic premise for spin coating of electromagnetic polymers, it focuses on fluid dynamics. To compute spin coating film thickness (h_f), the evaporation phenomenon must be included. The film coating thickness can be evaluated by balancing centrifugal force and evaporation, with thickness proportional to the inverse square root of spin speed ($h_f \ \alpha \ \omega^{-1/2}$). Generally, higher speeds (RPM) or higher viscosity result in thinner films. A variety of models exist for computing film thickness including the Emslie-Bonner-Peck model but it is limited to Newtonian fluids and also ignores effects of evaporation (which is linked to how volatile the solvent is) In this model the time rate of change of thickness, and radial rate of spreading can be computed, however. Another approach is the Meyerhofer Model which includes evaporation effects via a solvent evaporation rate. In this approach, early in the spin coating process, flow dominates the thinning process of the film (spin off); whereas later in the process (when the film is thinner and flow is slow), thinning is mainly due to evaporation. Meyerhofer also established that if the transition from fluid thinning to evaporation thinning is abrupt, then the film thickness can be estimated analytically – where it is assumed that the film is thin enough to ensure solvent concentration remains uniform through the depth of the film. Again, however this model is restricted to Newtonian coating liquids. For cases where the spin coating process is terminated early, the cross-over to evaporative thinning does not arise, and thickness and spin speed have a different relationship. In particular for non-Newtonian fluids which do not cross over to a Newtonian flow before being immobilised by evaporative thinning, the Meyerhofer Model fails. New models are required to correctly compute the film coating thickness with inclusion of evaporation. The maximum thickness that can be produced from a given material/solvent combination also depends upon the maximum concentration that the material can be dissolved in the solvent. For high solubility materials (100 mg/ml or higher), thicknesses of > 1 μm can be achieved. Meanwhile for some low solubility conjugated polymers (a few mg/ml) the maximum thickness might be limited to 20 nm or so. At low concentrations the thickness of a film is approximately linearly dependent upon the concentration of the material in the ink, however as concentrations increase this will affect the viscosity of the ink and thus a non-linear relationship will develop. Also, the range of spin speeds available is important as it defines the range of thicknesses that can be achieved from a given solution. In general, spin coating can produce uniform films relatively easily from about 1000 rpm upwards, but with care and attention good film quality can be achieved down to around 500 or 600 rpm in most cases (and even lower in some cases). Most common spin coaters will also reach a maximum speed of 6000 to 8000 rpm (although specialist coaters may go to 12000 rpm or higher). As such, a normal range of working spin coating rpm might span a factor of ten (from say 600 rpm to 6000 rpm) which in turn means a maximum variation in film thickness of around a factor 3.2. For example, a solution which gives a film thickness of 10 nm at 6000 rpm will give a thickness of around 32 nm at 600 rpm and if a thicker film is required then the solution concentration would need to be adjusted. In the reverse scenario, if a solution gives a thickness of 100 nm at 600 rpm, then the minimum thickness that can be achieved without diluting the solution will be 31.25 nm (100 / 3.2). In the present work we focus on momentum and thermal characteristics of the spin coating problem. Mass transfer and evaporation are not included but may be explored in the future based on the present platform built with the non-Newtonian magnetic polymer flow model analysis conducted in this paper, which is extensive, nevertheless.

The novelty of the present study is therefore the simultaneous consideration of viscous dissipation, Joule magnetic heating, Hall current and the combined Eyring–Powell micropolar non-Newtonian model for spin coating on a non-isothermal rotating cone. The non-dimensional equations with associated dimensionless boundary conditions constitute a highly nonlinear, coupled two-point boundary value problem. Keller's implicit finite difference "box" scheme is implemented to solve the problem [49]. In this study we probe the effects of the emerging thermophysical parameters, namely the Eyring-Powell rheological fluid parameter (ε), the local non-Newtonian parameter (δ), surface temperature exponent (*m*), Prandtl number (Pr), magnetic parameter (*M*), Hall current (β_e), Eckert number (Ec), Eringen micropolar fluid material parameters (V_1, λ), Eringen vortex viscosity parameter (*K*) and dimensionless tangential coordinate (ξ) on tangential and axial velocities, angular velocity (Eringen microrotation), temperature, skin friction and heat transfer rate (local Nusselt number) characteristics are studied. The motivation is to better understand the influence of these multiple parameters on the transport characteristics and establish which parameters induce more significant effects with implications in designing improve coatings. The present problem has to the authors' knowledge not appeared thus far in the scientific literature and is relevant to electromagnetic coating flows of multi-functional polymers, spin coating of UV light protection optical elements including curved gratings, anti-corrosion protective magnetic polymer coatings and magneto-sensitive thin-film amorphous silicon solar cell coatings etc.

In order to achieve this several key questions must be addressed:

(i) What are the relative influences of the different parameters on the velocity, angular velocity and temperature distributions in the boundary layer?

(ii) How are skin friction, wall couple stress (micro-rotation gradient) and Nusselt number influenced by combinations of viscoelastic, magnetic and radiative effects?

(iii) How are momentum, thermal and micro-rotation boundary layer thicknesses modified by multiple parameters in the simulations and what are the implications for magnetic rheological coating processing?

These questions are rigorously answered via the simulations and interpretation which provide new insights into the topic of electromagnetic non-Newtonian spin coating fluid dynamics.

2. Non-Newtonian Models Deployed in Magnetic Coating Simulation

2.1. Eyring-Powell fluid model

In the present study a subclass of non-Newtonian fluids known as the Eyring-Powell fluid is employed. The Cauchy stress tensor for Eyring-Powell fluids [50] takes the hyperbolic form:

$$\tau_{ij} = \mu \frac{\partial u_i}{\partial x_j} + \frac{1}{\beta}\sinh^{-1}\left(\frac{1}{C}\frac{\partial u_i}{\partial x_j}\right). \tag{1}$$

Considering the second-order approximation of the $\sinh^{-1}$ function as:

$$\sinh^{-1}\left(\frac{1}{C}\frac{\partial u_i}{\partial x_j}\right) \approx \frac{1}{C}\frac{\partial u_i}{\partial x_j} - \frac{1}{6}\left(\frac{1}{C}\frac{\partial u_i}{\partial x_j}\right)^3, \left|\frac{1}{C}\frac{\partial u_i}{\partial x_j}\right| < 1. \tag{2}$$

2.2. Eringen micropolar model

The balance equations for micropolar fluids [25] can be shown to take the vector form:

- ***Conservation of translational (linear) momentum***

$$(\lambda + 2\mu + k)\nabla\nabla \bullet V - (\mu + k)\nabla \times \nabla \times V + k\nabla \times G - \nabla p + \rho f = \rho V' \tag{3}$$

- ***Conservation of angular momentum (micro-rotation)***

$$\left(\alpha^* + \beta^* + \gamma\right)\nabla\nabla \bullet h - \gamma\nabla \times \nabla \times h + k\nabla \times V - 2kh + \rho l = \rho j h' \tag{4}$$

2.3. Combined magnetic polymer thermal spin coating Eringen-Eyring-Powell model

Amalgamating the constitutive models described in sections 2.1 and 2.2, we examine the steady, laminar, axisymmetric, electrically conducting, incompressible flow boundary layer flow of an Eyring-Powell micropolar magnetic polymer from a steadily revolving inverted cone with variable wall temperature, in an (x, y, z) coordinate system, as illustrated in Fig. 1.

The vertical cone is rotating at a constant angular velocity, (Ω), around its axis of symmetry. Fluid friction, including the no-slip condition, causes a circumferential velocity, w, of fluid elements, which are also subjected to a centrifugal force causing the radial velocity, v. Satisfying mass conservation, the outward-moving fluid is being replaced by fluid eventually flowing along the cone surface with velocity u. The applied magnetic field, B_0 is assumed to be static and uniform and acts radially i.e., normal to the cone surface. Ion slip and Maxwell displacement effects are ignored. The surface of the cone is electrically insulated and sustained at a variable temperature proportional to the power of the axial coordinate, x i.e., $T_w(x) = T_\infty + ax^m$, where a and m are constants. The gravitational acceleration, g, acts downwards. The magnetic Reynolds number is assumed to be small enough to neglect magnetic induction effects. The electron-atom collision frequency is assumed to be relatively high, so that the Hall current cannot be neglected [47, 48]. The Hall effect is the production of a potential difference (the Hall voltage) across an electrical conductor that is transverse to an electric current in the conductor and to an applied magnetic field perpendicular to the current. It is a characteristic of the material from which the conductor is made, since its value depends on the type, number, and properties of the charge carriers that constitute the current.

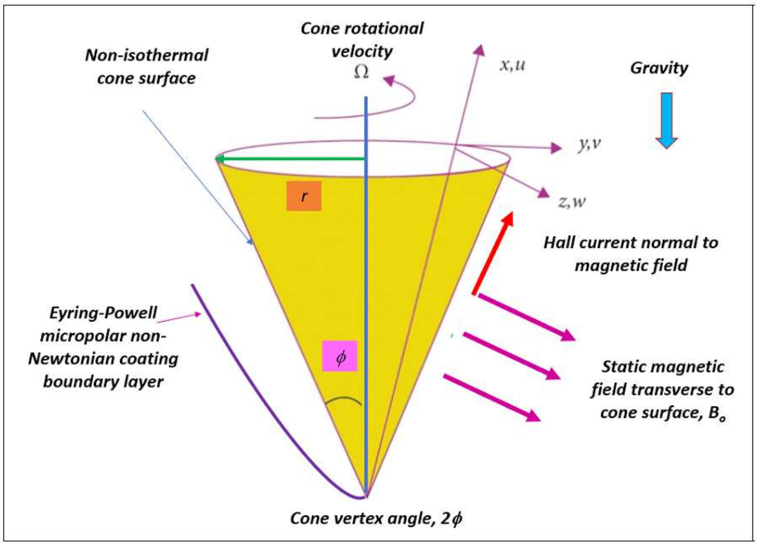

Fig. 1. Non-Newtonian electroconductive polymer layer flow from a spinning inverted cone.

The appropriate electromagnetic equations are as follows [51]:

- Ohm's law for moving conductor with Hall currents

$$J + \frac{\omega_e \tau_e}{B_0}(J \times B) = \sigma(E + q \times B) \tag{5}$$

- Maxwell electromagnetic equations

$$\vec{\nabla} \cdot B = \mu_e J \tag{6}$$

$$\vec{\nabla} \cdot E = -\frac{\partial B}{\partial t} \tag{7}$$

$$\vec{\nabla} \cdot J \neq 0 \tag{8}$$

$$\vec{\nabla} \cdot B = 0 \tag{9}$$

Here $\boldsymbol{q}$ is the velocity vector $(\bar{u}, \bar{v}, \bar{w})$, $J = (J_r, J_\theta, J_z)$ is the electrical density vector, $\boldsymbol{B}$ is the magnetic field vector, $\boldsymbol{E}$ is the electrical field vector, ω_e, σ, τ_e are electron frequency, electrical conductivity and electron collision time, respectively. Furthermore, μ_e *is the magnetic permeability* of the fluid. Since there exists no applied or polarization voltage on the magnetic polymer flow field, and the cone surface is electrically insulated, the electric field vector vanishes i.e., $E = 0$. It follows that the current density has components J_x and J_z as follows, where B_z is taken as B_0 :

$$J_x = \frac{\sigma B_0^2}{(1 + h^2)\rho}(\bar{u} - h\bar{v}) \tag{10}$$

$$J_z = \frac{\sigma B_0^2}{(1 + h^2)\rho}(\bar{v} + h\bar{u}) \tag{11}$$

Here $h = \omega_e \tau_e$ is the dimensional Hall parameter. Under these assumptions, the boundary layer equations under Boussinesq approximation may be written by extending and combining the models of Abo-Eldahab and Elaziz [52] and Powell and Eyring [50] as follows:

$$\frac{\partial(ru)}{\partial x} + \frac{\partial(rv)}{\partial y} = 0 \tag{12}$$

$$u\frac{\partial u}{\partial x} + v\frac{\partial u}{\partial y} - \frac{w^2}{x} = \left(\nu + \frac{k}{\rho} + \frac{1}{\rho\beta C}\right)\frac{\partial^2 u}{\partial y^2} - \frac{1}{6\rho\beta C^3}\left(\frac{\partial u}{\partial y}\right)^2 \frac{\partial^2 u}{\partial y^2} + g_1\beta_1(T - T_\infty)\cos\varphi + \frac{k}{\rho}\frac{\partial N}{\partial y} - \frac{\sigma B_0^2}{\rho(1 + \beta_e^2)}(u + \beta_e w). \tag{13}$$

$$u\frac{\partial w}{\partial x} + v\frac{\partial w}{\partial y} + \frac{uw}{x} = \left(\nu + \frac{k}{\rho} + \frac{1}{\rho\beta C}\right)\frac{\partial^2 w}{\partial y^2} - \frac{1}{6\rho\beta C^3}\left(\frac{\partial w}{\partial y}\right)^2 \frac{\partial^2 w}{\partial y^2} + \frac{\sigma B_0^2}{\rho(1 + \beta_e^2)}(\beta_e u - w). \tag{14}$$

$$u\frac{\partial N}{\partial x} + v\frac{\partial N}{\partial y} + \frac{uN}{x} = \frac{\gamma}{\rho j}\frac{\partial^2 N}{\partial y^2} - \frac{k}{\rho j}\left(2N + \frac{\partial u}{\partial y}\right). \tag{15}$$

$$u\frac{\partial T}{\partial x} + v\frac{\partial T}{\partial y} = \alpha\frac{\partial^2 T}{\partial y^2} + \frac{\sigma B_0^2}{\rho c_p(1 + \beta_e^2)}(u^2 + w^2). \tag{16}$$

The corresponding boundary conditions imposed at the cone surface (wall) and in the freestream (edge of the boundary layer) are:

$$\begin{aligned} &\text{At } y = 0, \quad u = v = 0, \quad w = r\Omega, \quad N = -\frac{1}{2}\frac{\partial u}{\partial y}, \quad T = T_w(x). \\ &\text{As } y \to \infty, \quad u \to 0, \quad v \to 0, \quad w \to 0, \quad N \to 0, \quad T \to T_\infty. \end{aligned} \tag{17}$$

The dimensional stream function ψ is defined by $ru = \partial\psi/\partial y$ and $rv = -\partial\psi/\partial x$, and therefore, the continuity equation is automatically satisfied.

In order to render the governing equations and the boundary conditions in dimensionless form, the following non-dimensional quantities are introduced:

$$\begin{aligned} &\xi = \frac{\zeta}{1+\zeta}, \quad \eta = \frac{y}{x}\chi, \quad \psi = r\alpha\chi f, \quad g(\xi,\eta) = \frac{w}{r\Omega}, \quad \theta(\xi,\eta) = \frac{T - T_\infty}{T_w - T_\infty}, \quad r(x) = x\sin\varphi \\ &h(\xi,\eta) = \frac{\nu x^2}{\alpha^2\chi^3}N, \ \zeta = \frac{Re^{1/2}}{Ra^{1/4}}, \ Re = \frac{x^2\Omega\sin\varphi}{\nu}, \ Ra = \frac{g\beta(T_w - T_\infty)x^3\cos\varphi}{\alpha\nu}, \ \chi = \frac{Re^{1/2}}{\xi} \end{aligned} \tag{18}$$

Utilizing the transformations (18), the boundary layer Eqs. (13) - (17) emerge as the following nonlinear, dimensionless boundary layer equations in a (ξ,η) coordinate system:

$$\begin{aligned}&\Pr(1+K+\varepsilon)f'''-\Pr\varepsilon\delta(f'')^2 f'''+\left(2-\frac{(1-\xi)(1-m)}{4}\right)ff''-\left(1-\frac{(1-\xi)(1-m)}{2}\right)(f')^2+\Pr^2\xi^4 g^2+\Pr(1-\xi)^4\theta+Kh'\\&-\frac{\Pr M\xi^2}{1+\beta_e^2}(f'+\beta_e\Pr\xi^2 g)=\xi(1-\xi)\left(\frac{1-m}{4}\right)\left(f'\frac{\partial f'}{\partial\xi}-f''\frac{\partial f}{\partial\xi}\right).\end{aligned} \tag{19}$$

$$\Pr(1+K+\varepsilon)g''-\Pr^3\varepsilon\delta\xi^4(g')^2 g''+\left(2-\frac{(1-\xi)(1-m)}{4}\right)fg'-2gf'+\frac{M}{1+\beta_e^2}(\beta_e f'-\Pr\xi^2 g)=\xi(1-\xi)\left(\frac{1-m}{4}\right)\left(f'\frac{\partial g}{\partial\xi}-g'\frac{\partial f}{\partial\xi}\right). \tag{20}$$

$$\Pr\lambda h''+\left(2-\frac{(1-\xi)(1-m)}{4}\right)fh'-\left(2-\frac{3(1-\xi)(1-m)}{4}\right)hf'-\Pr KV_1\xi^2\,(2h+\Pr f'')=\xi(1-\xi)\left(\frac{1-m}{4}\right)\left(f'\frac{\partial h}{\partial\xi}-h'\frac{\partial f}{\partial\xi}\right). \tag{21}$$

$$\theta''+\left(2-\frac{(1-\xi)(1-m)}{4}\right)f\theta'-mf'\theta+\frac{Ec.M}{1+\beta_e^2}\left(f'^2+\Pr^2\xi^4 g^2\right)=\xi(1-\xi)\left(\frac{1-m}{4}\right)\left(f'\frac{\partial\theta}{\partial\xi}-\theta'\frac{\partial f}{\partial\xi}\right). \tag{22}$$

The transformed dimensionless boundary conditions take the form:

$$\begin{aligned}&\text{At}\quad \eta=0,\quad f=0,\quad f'=0,\quad g=1,\quad h=-\frac{\Pr}{2}f'',\quad \theta=1.\\&\text{As}\quad \eta\to\infty,\quad f'\to 0,\quad g\to 0,\quad h\to 0,\quad \theta\to 0.\end{aligned} \tag{23}$$

Here primes denote the differentiation with respect to η, and the dimensionless control parameters in Eqs. (19 – 22) are defined: as: $K=k/\mu$, $\lambda=\gamma/j\mu$, $V_1=\nu/j\Omega\sin\varphi$, $\Pr=\nu/\alpha$, $\varepsilon=1/\mu\beta C$, $\delta=\alpha^2\lambda^6/6C^2x^4$, $M=\sigma B_0^2/\rho\Omega\sin\varphi$, $Ec=\rho\Omega\sin\varphi/c_p(T_w-T_\infty)$.

The skin-friction coefficients (shear stresses at the cone surface), wall couple stress and Nusselt number (heat transfer rate) can be defined using the transformations in Eq. (18) by following expressions:

$$C_{fx}=\left(1+\frac{K}{2}+\varepsilon\right)f''(\xi,0)-\varepsilon\delta\left(f''(\xi,0)\right)^3+\frac{K}{\Pr}h. \tag{24}$$

$$C_{gx}=\left(1+\frac{K}{2}+\varepsilon\right)\xi^2 g'(\xi,0)-\Pr^2\varepsilon\delta\xi^6\left(g'(\xi,0)\right)^3. \tag{25}$$

$$Wcs=\Pr\left(1+\frac{K}{2}\right)h'. \tag{26}$$

$$Nu=-\theta'(\xi,0). \tag{27}$$

The location, $\xi\sim 0$, corresponds to the vicinity of the lower stagnation point on the cone. In this case, the boundary value problem Eqs. (12) – (15) reduce to the special case of an ordinary differential boundary value problem:

$$\Pr(1+K+\varepsilon)f'''-\Pr\varepsilon\delta(f'')^2 f'''+\left(2-\frac{1-m}{4}\right)ff''-\left(1-\frac{1-m}{2}\right)f'^2+\Pr\theta+Kh'=0. \tag{28}$$

$$\Pr(1+K+\varepsilon)g''-+\left(2-\frac{1-m}{4}\right)fg'-2gf'+\frac{M}{1+\beta_e^2}(\beta_e f')=0. \tag{29}$$

$$\Pr\lambda h''+\left(2-\frac{1-m}{4}\right)fh'-\left(2-\frac{3(1-m)}{4}\right)hf'=0. \tag{30}$$

$$\theta''+\left(2-\frac{1-m}{4}\right)f\theta'-mf'\theta+\frac{EcM}{1+\beta_e^2}\left(f'^2\right)=0. \tag{31}$$

3. Computational Solution and Verification

Equations (19) – (22) under boundary conditions (23) have been solved computationally with Keller-box method [49] has a second order accuracy with arbitrary spacing and attractive extrapolation features. This technique is exceptionally stable and converges quickly. It is ideal for two-point boundary value problems and has been applied in many complex flow regimes including electromagnetic nanofluid enclosure dynamics [52], magnetic functional nanopolymer coating flows [53] and Hall magneto-nanofluid dynamics [54]. A uniform spaced mesh is deployed in the computations which are executed using an in-house code in the MATLAB platform. The Keller Box Scheme comprises four stages.

1) Decomposition of the N^{th} order partial differential equation system to N first order equations.
2) Finite difference discretization.
3) Quasi-linearization of non-linear Keller algebraic equations.
4) Block-tridiagonal elimination solution of the linearized Keller algebraic equations.

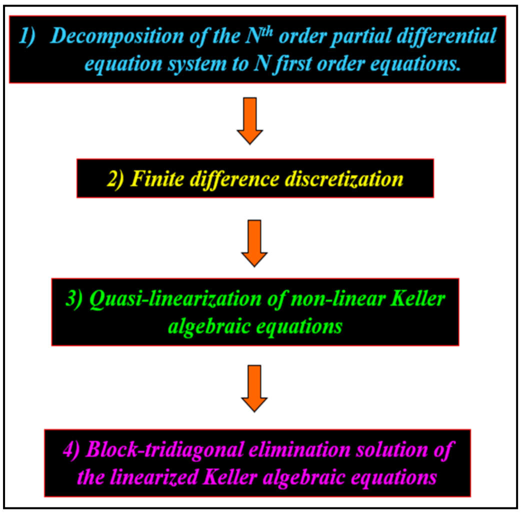

Fig. 2. Stages involved in the Keller box implicit finite difference scheme.

The methodology is summarized as per the MATLAB-based in-house code along with a representative Keller box (cell) and boundary layer grid design in Fig. 2.

Step 1: Decomposition of the N^{th} order partial differential equation system to N first order equations;

New variables are introduced to Eqs. (19) - (22) and (23), to render the boundary value problem as a multiple system of first order equations. A set of nine simultaneous first order differential equations are therefore generated:

$$u(x,y)=f',\quad v(x,y)=f'',\quad g'(x,y)=p,\quad q(x,y)=h',\quad s(x,y)=\theta,\quad t(x,y)=\theta' \tag{32}$$

$$f'=u \tag{33}$$

$$u'=v \tag{34}$$

$$g'=p \tag{35}$$

$$h'=q \tag{36}$$

$$s'=t \tag{37}$$

$$\begin{aligned}&\Pr(1+K+\varepsilon)v'-\Pr\varepsilon\delta v^2v'+\left(2-\frac{(1-\xi)(1-m)}{4}\right)fv-\left(1-\frac{(1-\xi)(1-m)}{2}\right)u^2+\Pr^2\xi^4g^2+\Pr(1-\xi)^4\theta+Kq-\frac{\Pr M\xi^2}{1+\beta_e^2}\left(u+\beta_e\Pr\xi^2 g\right)\\&=\xi(1-\xi)\left(\frac{1-m}{4}\right)\left(u\frac{\partial u}{\partial\xi}-v\frac{\partial f}{\partial\xi}\right).\end{aligned} \tag{38}$$

$$\Pr(1+K+\varepsilon)p'-\Pr^3\varepsilon\delta\xi^4p^2p'+\left(2-\frac{(1-\xi)(1-m)}{4}\right)fp-2gu+\frac{M}{1+\beta_e^2}\left(\beta_e u-\Pr\xi^2 g\right)=\xi(1-\xi)\left(\frac{1-m}{4}\right)\left(u\frac{\partial g}{\partial\xi}-p\frac{\partial f}{\partial\xi}\right). \tag{39}$$

$$\Pr\lambda q'+\left(2-\frac{(1-\xi)(1-m)}{4}\right)fq-\left(2-\frac{3(1-\xi)(1-m)}{4}\right)hu-\Pr K V_1\xi^2\,(2h+\Pr v)=\xi(1-\xi)\left(\frac{1-m}{4}\right)\left(u\frac{\partial h}{\partial\xi}-q\frac{\partial f}{\partial\xi}\right). \tag{40}$$

$$t'+\left(2-\frac{(1-\xi)(1-m)}{4}\right)ft-mus+\frac{Ec.M}{1+\beta_e^2}\left(u^2+\Pr^2\xi^4g^2\right)=\xi(1-\xi)\left(\frac{1-m}{4}\right)\left(u\frac{\partial s}{\partial\xi}-t\frac{\partial f}{\partial\xi}\right). \tag{41}$$

The transformed dimensionless boundary conditions take the form:

$$\begin{aligned}&\text{At}\quad \eta=0,\quad f=0,\quad u=0,\quad g=1,\quad h=-\frac{\Pr}{2}f'',\quad s=1.\\&\text{As}\quad \eta\to\infty,\quad u\to 0,\quad g\to 0,\quad h\to 0,\quad s\to 0.\end{aligned} \tag{42}$$

Step 2: Finite difference discretization;

A two-dimensional computational grid is imposed on the $\xi-\eta$ plane as sketched in Fig. 3. The stepping process is defined by:

$$\begin{aligned}&\eta_0=0,\quad \eta_j=\eta_{j-1}+h_j,\quad j=1,2,\dots,J,\quad \eta_J=\eta_\infty\\&\xi^0=0,\quad \xi^n=\xi^{n-1}+k_n,\quad n=1,2,\dots,N\end{aligned} \tag{43}$$

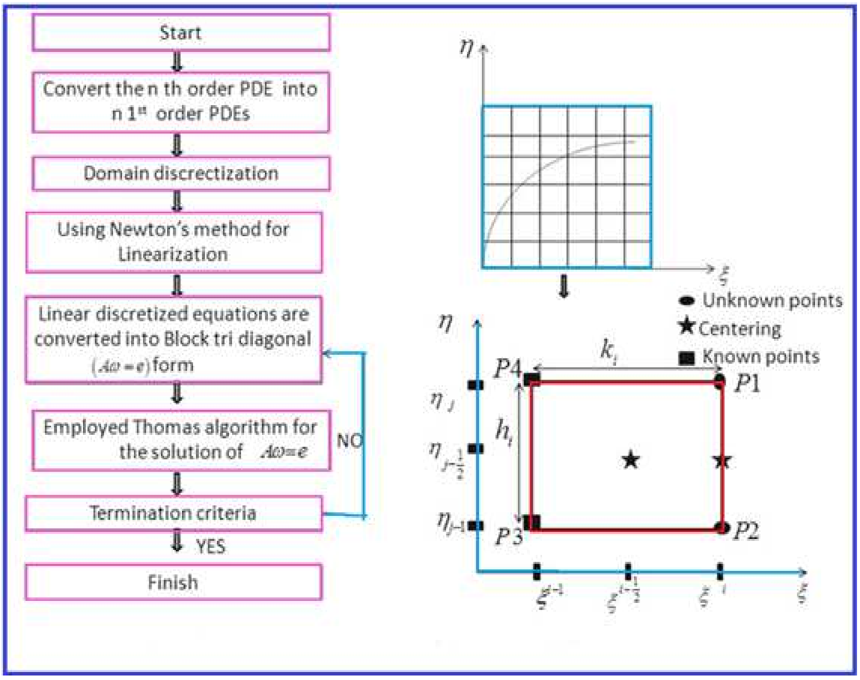

Fig. 3. Keller Box Procedure, Box cell and boundary layer meshing.

where k_n is the $\Delta\xi$ - spacing and h_j is the $\Delta\eta$ - spacing. If g_j^n denotes the value of any variable at (η_j, ξ^n), then the variables and derivatives of Eqs. (33) – (42) at $(\eta_{j-1/2}, \xi^{n-1/2})$ are replaced by:

$$g_{j-1/2}^{n-1/2} = \frac{1}{4}\left(g_j^n + g_{j-1}^n + g_j^{n-1} + g_{j-1}^{n-1}\right) \tag{44}$$

$$\left(\frac{\partial g}{\partial \eta}\right)_{j-1/2}^{n-1/2} = \frac{1}{2h_j}\left(g_j^n - g_{j-1}^n + g_j^{n-1} - g_{j-1}^{n-1}\right) \tag{45}$$

$$\left(\frac{\partial g}{\partial \xi}\right)_{j-1/2}^{n-1/2} = \frac{1}{2k^n}\left(g_j^n - g_{j-1}^n + g_j^{n-1} - g_{j-1}^{n-1}\right) \tag{46}$$

The resulting finite-difference approximation of Eqs. (33) – (42) for the mid – point $(\eta_{j-1/2}, \xi^n)$, are:

$$h_j^{-1}\left(f_j^n - f_{j-1}^n\right) = u_{j-1/2}^n \tag{47}$$

$$h_j^{-1}\left(u_j^n - u_{j-1}^n\right) = v_{j-1/2}^n \tag{48}$$

$$h_j^{-1}\left(g_j^n - g_{j-1}^n\right) = p_{j-1/2}^n \tag{49}$$

$$h_j^{-1}\left(h_j^n - h_{j-1}^n\right) = q_{j-1/2}^n \tag{50}$$

$$h_j^{-1}\left(s_j^n - s_{j-1}^n\right) = t_{j-1/2}^n \tag{51}$$

$$\begin{aligned}
&\Pr(1+K+\varepsilon)\left(v_j - v_{j-1}\right) - \frac{\Pr\varepsilon\delta}{4}\left(v_j + v_{j-1}\right)^2\left(v_j - v_{j-1}\right) + \left[2 - \frac{(1-\xi)(1-m)}{4} + \frac{\alpha(1-\alpha)(1-m)}{4}\right]\frac{h_j}{4}\left(f_j + f_{j-1}\right)\left(v_j + v_{j-1}\right) \\
&-\left[1 - \frac{(1-\xi)(1-m)}{2} + \frac{\alpha(1-\alpha)(1-m)}{4}\right]\frac{h_j}{4}\left(u_j + u_{j-1}\right)^2 + \Pr^2\xi^4\frac{h_j}{4}\left(g_j + g_{j-1}\right)^2 + \Pr(1-\xi)^4\frac{h_j}{2}\left(s_j + s_{j-1}\right) + K\frac{h_j}{2}\left(q_j + q_{j-1}\right) \\
&-\frac{\Pr M\xi^2}{1+\beta_e^2}\frac{h_j}{2}\left(\left(u_j + u_{j-1}\right) + \beta_e \Pr\xi^2\left(g_j + g_{j-1}\right)\right) - \frac{\alpha(1-\alpha)(1-m)h_j}{8}\left(f_{j-1/2}^{n-1}\left(v_j + v_{j-1}\right) - v_{j-1/2}^{n-1}\left(f_j + f_{j-1}\right)\right) = [R_1]_{j-/12}^{n-1}.
\end{aligned} \tag{52}$$

$$\begin{aligned}
&\Pr(1+K+\varepsilon)\left(p_j - p_{j-1}\right) - \frac{\Pr\varepsilon\delta}{4}\left(p_j + p_{j-1}\right)^2\left(p_j - p_{j-1}\right) + \left[2 - \frac{(1-\xi)(1-m)}{4} + \frac{\alpha(1-\alpha)(1-m)}{4}\right]\frac{h_j}{4}\left(f_j + f_{j-1}\right)\left(p_j + p_{j-1}\right) \\
&-\left[2 + \frac{\alpha(1-\alpha)(1-m)}{4}\right]\frac{h_j}{4}\left(g_j + g_{j-1}\right)\left(u_j + u_{j-1}\right) + \frac{M}{1+\beta_e^2}\frac{h_j}{2}\left(\beta_e\left(u_j + u_{j-1}\right) - \Pr\xi^2\left(g_j + g_{j-1}\right)\right) \\
&+\frac{\alpha(1-\alpha)(1-m)h_j}{8}\left(g_{j-1/2}^{n-1}\left(u_j + u_{j-1}\right) - u_{j-1/2}^{n-1}\left(g_j + g_{j-1}\right) - f_{j-1/2}^{n-1}\left(p_j + p_{j-1}\right) + p_{j-1/2}^{n-1}\left(f_j + f_{j-1}\right)\right) = [R_2]_{j-/12}^{n-1}.
\end{aligned} \tag{53}$$

$$\begin{aligned}&\Pr\lambda\left(q_j-q_{j-1}\right)+\left[2-\frac{(1-\xi)(1-m)}{4}+\frac{\alpha(1-\alpha)(1-m)}{4}\right]\frac{h_j}{4}\left(f_j+f_{j-1}\right)\left(q_j+q_{j-1}\right)\\&-\left[2-\frac{3(1-\xi)(1-m)}{4}+\frac{\alpha(1-\alpha)(1-m)}{4}\right]\frac{h_j}{4}\left(h_j+h_{j-1}\right)\left(u_j+u_{j-1}\right)-\Pr K V_1\xi^2\frac{h_j}{2}\left(2\left(h_j+h_{j-1}\right)+\Pr\left(v_j+v_{j-1}\right)\right)\\&+\frac{\alpha(1-\alpha)(1-m)h_j}{8}\left(h_{j-1/2}^{n-1}\left(u_j+u_{j-1}\right)-u_{j-1/2}^{n-1}\left(h_j+h_{j-1}\right)-f_{j-1/2}^{n-1}\left(q_j+q_{j-1}\right)+q_{j-1/2}^{n-1}\left(f_j+f_{j-1}\right)\right)=[R_3]_{j-/12}^{n-1}.\end{aligned}\tag{54}$$

$$\begin{aligned}&\left(t_j-t_{j-1}\right)+\left[2-\frac{(1-\xi)(1-m)}{4}+\frac{\alpha(1-\alpha)(1-m)}{4}\right]\frac{h_j}{4}\left(f_j+f_{j-1}\right)\left(t_j+t_{j-1}\right)\\&-\left[m+\frac{\alpha(1-\alpha)(1-m)}{4}\right]\frac{h_j}{4}\left(s_j+s_{j-1}\right)\left(u_j+u_{j-1}\right)-\frac{Ec.M}{1+\beta_e^2}\frac{h_j}{4}\left(\left(u_j+u_{j-1}\right)^2+\Pr^2\xi^4\left(g_j+g_{j-1}\right)^2\right)\\&+\frac{\alpha(1-\alpha)(1-m)h_j}{8}\left(s_{j-1/2}^{n-1}\left(u_j+u_{j-1}\right)-u_{j-1/2}^{n-1}\left(s_j+s_{j-1}\right)-f_{j-1/2}^{n-1}\left(t_j+t_{j-1}\right)+t_{j-1/2}^{n-1}\left(f_j+f_{j-1}\right)\right)=[R_4]_{j-/12}^{n-1}.\end{aligned}\tag{55}$$

where we have used the abbreviations:

$$[R_1]_{j-1/2}^{n-1}=-h_j\left[\begin{aligned}&\Pr(1+K+\varepsilon)(v')_{j-1/2}^{n-1}+\left(2-\frac{(1-\xi)(1-m)}{4}-\frac{\alpha(1-\alpha)(1-m)}{4}\right)(fv)_{j-1/2}^{n-1}-\left(1-\frac{(1-\xi)(1-m)}{2}-\frac{\alpha(1-\alpha)(1-m)}{4}\right)\left(u_{j-1}^{n-1}\right)^2\\&-\Pr\varepsilon\delta\left(v^2v'\right)_{j-1/2}^{n-1}+Kq_{j-1}^{n-1}+\Pr^2\xi^4\left(g_{j-1}^{n-1}\right)^2+\Pr(1-\xi)^4 s_{j-1}^{n-1}-\frac{M.\Pr.\xi^2}{1+\beta_e^2}\left(u_{j-1/2}^{n-1}+\beta_e\Pr\xi^2 g_{j-1/2}^{n-1}\right)\end{aligned}\right]\tag{56}$$

$$[R_2]_{j-1/2}^{n-1}=-h_j\left[\begin{aligned}&\Pr(1+K+\varepsilon)(p')_{j-1/2}^{n-1}+\left(2-\frac{(1-\xi)(1-m)}{4}-\frac{\alpha(1-\alpha)(1-m)}{4}\right)(fp)_{j-1/2}^{n-1}-\left(2-\frac{\alpha(1-\alpha)(1-m)}{4}\right)(gu)_{j-1/2}^{n-1}\\&-\Pr^3\varepsilon\delta\xi^4\left(p^2p'\right)_{j-1/2}^{n-1}+\frac{M}{1+\beta_e^2}\left(\beta_e u_{j-1/2}^{n-1}-\Pr\xi^2 g_{j-1/2}^{n-1}\right)\end{aligned}\right]\tag{57}$$

$$[R_3]_{j-1/2}^{n-1}=-h_j\left[\begin{aligned}&\Pr\lambda(q')_{j-1/2}^{n-1}+\left(2-\frac{(1-\xi)(1-m)}{4}-\frac{\alpha(1-\alpha)(1-m)}{4}\right)(fq)_{j-1/2}^{n-1}\\&-\left(2-\frac{3(1-\xi)(1-m)}{4}-\frac{\alpha(1-\alpha)(1-m)}{4}\right)(hu)_{j-1/2}^{n-1}-\Pr KV_1\left(2h_{j-1/2}^{n-1}+\Pr v_{j-1/2}^{n-1}\right)\end{aligned}\right]\tag{58}$$

$$[R_4]_{j-1/2}^{n-1}=-h_j\left[\begin{aligned}&(t')_{j-1/2}^{n-1}+\left(2-\frac{(1-\xi)(1-m)}{4}-\frac{\alpha(1-\alpha)(1-m)}{4}\right)(ft)_{j-1/2}^{n-1}\\&-\left(m-\frac{\alpha(1-\alpha)(1-m)}{4}\right)(us)_{j-1/2}^{n-1}+\frac{Ec.M}{1+\beta_e^2}\left(\left(u^2\right)_{j-1/2}^{n-1}+\Pr^2\xi^4\left(g^2\right)_{j-1/2}^{n-1}\right)\end{aligned}\right]\tag{59}$$

The boundary conditions are:

$$f_0^n=u_0^n=0,\quad s_0^n=1,\quad g_0^n=-\frac{1}{2}v_0^2,\quad u_J^n=0,\quad v_J^n=0,\quad s_J^n=0,\quad g_J^n=0\tag{60}$$

Step 3: Quasilinearization of non-linear Keller algebraic equations; If we assume $f_j^{n-1},u_j^{n-1},v_j^{n-1},q_j^{n-1},g_j^{n-1},p_j^{n-1},s_j^{n-1},t_j^{n-1}$ to be known for $0\le j\le J$, this leads to a system of $9J+9$ equations for the solution of unknowns $f_j^n,u_j^n,v_j^n,q_j^n,h_j^n,g_j^n,p_j^n,s_j^n,t_j^n$, $j=0,1,2,...,J$. This non-linear system of algebraic equations is linearized by means of Newton's method.

Step 4: Block-tridiagonal elimination solution of linear Keller algebraic equations; The linearized system is solved by the block-elimination method, since it possesses a block-tridiagonal structure. The block-tridiagonal structure generated consists of *block matrices*. The complete linearized system is formulated as a *block matrix system*, where each element in the coefficient matrix is a matrix itself, and this system is solved using the efficient Keller-box method. The numerical results are strongly influenced by the number of mesh points in both directions. After some trials in the η -direction (radial coordinate) a larger number of mesh points are selected whereas in the ξ -direction (tangential coordinate) significantly less mesh points are utilized. $\eta_{\max}$ has been set at 30 and this defines an adequately large value at which the prescribed boundary conditions are satisfied. $\xi_{\max}$ is set at 1 for this flow domain. Mesh independence is achieved in the present computations. The numerical algorithm is executed in MATLAB on a PC. The method demonstrates excellent stability, convergence and consistency, as elaborated by Keller [49].

Convergence Analysis: The calculations are repeated until some convergence criterion is satisfied. In laminar boundary layer calculations, the wall shear stress parameter, $v(x,0)$, is commonly used as the convergence criterion [51]. In boundary layer calculations, it is found that the greatest error usually appears in the wall shear stress parameter. It is worth mentioning that throughout the course of this study, this convergence criterion is used as it is efficient, suitable and the best yet for all the problems considered. Calculations are stopped when $|\delta v_0^{(i)}|<\varepsilon_1$, where ε_1 is a small, prescribed value.

Validation: To validate the accuracy of the code, benchmarking with the earlier study of Eldahab and Elaziz [52], in the absence of Eyring-Powell effects i.e., $\varepsilon=\delta=0$. Table 1 gives the comparison for Nusselt number, $Nu=-\theta'(\xi,0)$ with the solutions in [52] for various values of magnetic interaction parameter *M*, Hall parameter β_e and Eckert number *Ec*, both at the vertex point *i.e.* boundary layer leading edge $(\xi=0)$ and also further along the slant surface from the cone vertex $(\xi=1)$. Excellent correlation is achieved testifying to the accuracy of the Keller box code.

Table 1. Comparison values of $-\theta'(\xi,0)$ for various values of M, β_e and Ec when λ = K = 0.5, m = 2, Pr = 1 and V_1 = 0.1.

M	β_e	Ec	$\xi=0$		$\xi=1$	
			Eldahab and Elaziz [52]	Keller Box	Eldahab and Elaziz [52]	Keller Box
0.0			0.69338	0.69336	0.62986	0.62985
0.5	0.2		0.68652	0.68651	0.34940	0.34938
1.0		0.5	0.67934	0.67932	0.12904	0.12902
	0.2		0.67934	0.67932	0.12904	0.12902
	1.0		0.68624	0.68622	0.45938	0.45935
1.0	1.5		0.68903	0.68901	0.55746	0.55744
		0.0	0.69338	0.69336	0.47751	0.47748
	0.2	0.5	0.67934	0.67933	0.12904	0.12902
		1.0	0.66394	0.66392	-0.24731	-0.24728

4. Computational Results and Discussion

Graphical plots of the influence of key control parameters on axial velocity (f'), tangential velocity (g), angular velocity (h) and temperature (θ) distributions through the boundary layer regime are visualized in Figs. 4 - 22. Additionally, solutions for axial skin friction (C_{fx}), tangential skin friction (C_{gx}), wall couple stress (micro-rotation gradient at the cone surface) (Wcs) and Nusselt number (Nu) are presented in Tables 2 and 3. Eleven thermo-physical and body force control parameters feature in the model, namely, ε, δ, m, M, Pr, Ec, V_1, λ, β_e, K, ξ. The following default parameter values are used: $\varepsilon=\delta=0.3$, $m=1$, $\mathrm{Pr}=7$, $V_1=0.2$, $M=Ec=\lambda=\beta_e=0.5$, $K=3$, $\xi=1.0$. This data is taken from suitable sources for practical applications of magnetic non-Newtonian coatings [46, 47]. Furthermore, the influence of stream-wise (transverse) coordinate on heat transfer characteristics is also investigated.

Figures 4 to 7 present the effects of *first rheological fluid parameter,* ε on the axial velocity (f'), tangential velocity (g), angular velocity (h) and temperature (θ) distributions through the boundary layer regime. Figure 4 shows the impact of power-law rheological index on axial velocity evolution with transverse coordinate (η). The Eyring-Powell model effectively introduces two non-Newtonian parameters into the boundary layer equations, ε, δ, each of which has a different role. The first parameter, $\varepsilon=1/\mu\beta C$ is inversely proportional to the dynamic viscosity of the magnetic polymer and features in the augmented shear terms, $\mathrm{Pr}(1+K+\varepsilon)f'''-\mathrm{Pr}\,\varepsilon\,\delta(f'')^2 f'''$ in the axial momentum Eq. (19). In the case where $\varepsilon=\delta=0$, the Eyring-Powell rheological effects are removed and only a micropolar fluid is present. An elevation in ε exerts a different influence depending on the location relative to the cone surface $(\eta=0)$. Closer to the wall (cone surface) as ε *is increased,* there is a weak acceleration induced in the axial flow *i.e.* axial velocities are enhanced. Beyond a critical distance however from the wall, the reverse pattern is computed and increasing first Eyring-Powell rheological parameter produces a significant deceleration in the axial flow which is sustained into the freestream. Clearly with larger ε, *the dynamic viscosity is reduced as per the definition of this parameter*. This leads to the acceleration initially in the axial flow in close proximity to the cone surface (wall). However, the other Eyring-Powell material parameters, β *and* C also contribute as ε *is modified and effectively deceleration is produced for the majority of the boundary layer region into the free stream*. Asymptotically smooth profiles are computed in the free stream confirming the prescription of an adequately large infinity boundary condition in the Keller box numerical code.

Figure 5 demonstrates that a very different response is computed in tangential velocity (g) with increasing first Eyring-Powell rheological parameter. A strong acceleration is computed throughout the boundary layer regime from the wall to the freestream. The destruction in axial momentum is compensated for by the re-distribution in momentum in the tangential direction. This leads to a sustained elevation in tangential velocities in the rotating boundary layer regime. A direct influence is also experienced on the tangential momentum boundary layer Eq. (20) via the terms, $\mathrm{Pr}(1+K+\varepsilon)g''$, although it is less prominent than on the axial (primary) momentum Eq. (19). There will also be a spiraling interaction between the axial and tangential boundary layer growth during the rotation of the cone. It is important to note that consistently positive values of both axial and tangential velocities are achieved at all values of ε *confirming that back flow is never present in the swirling regime.*

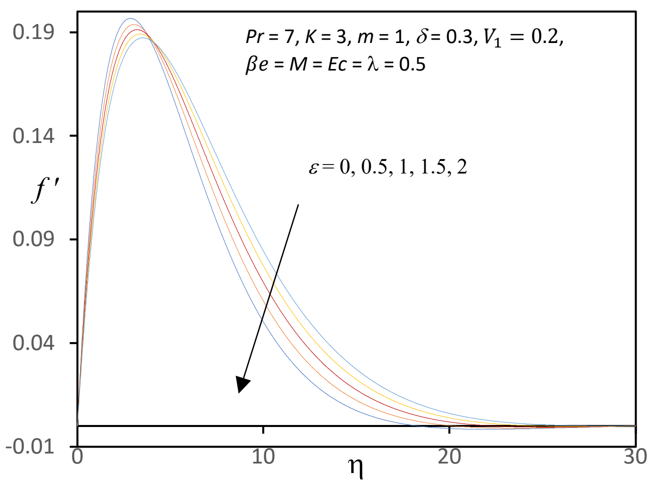

Fig. 4. Influence of ε on axial velocity profiles.

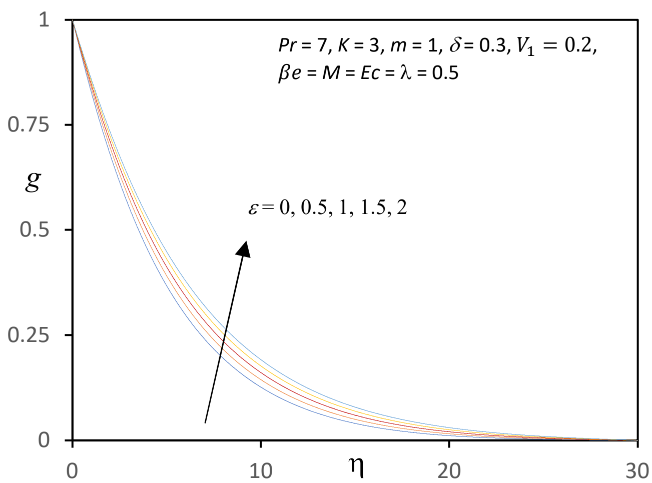

Fig. 5. Influence of ε on tangential velocity profiles.

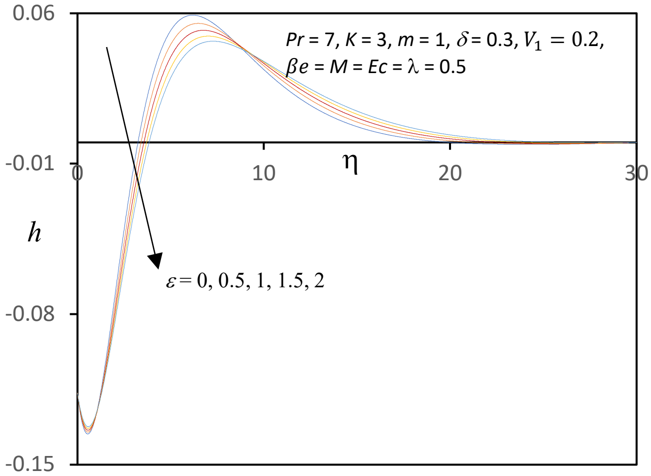

Fig. 6. Influence of ε on angular velocity profiles.

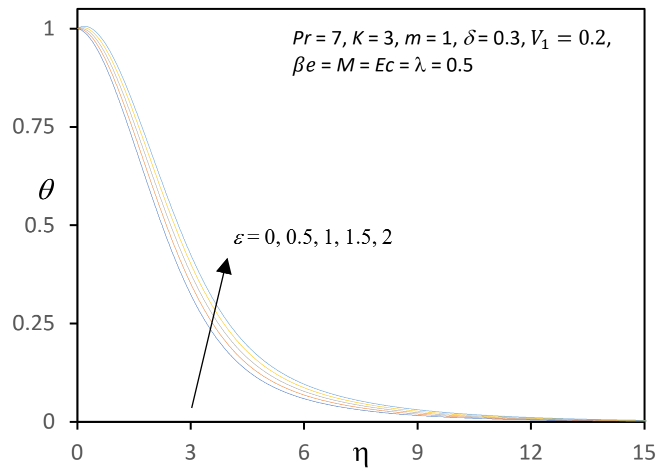

Fig. 7. Influence of ε on temperature profiles.

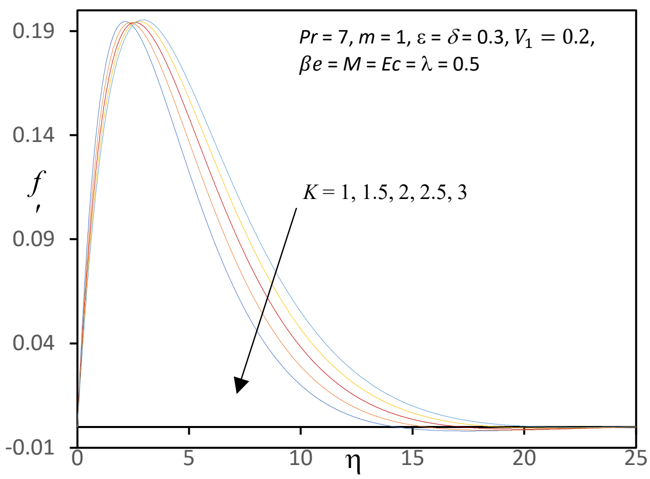

Fig. 8. Influence of K on axial velocity profiles.

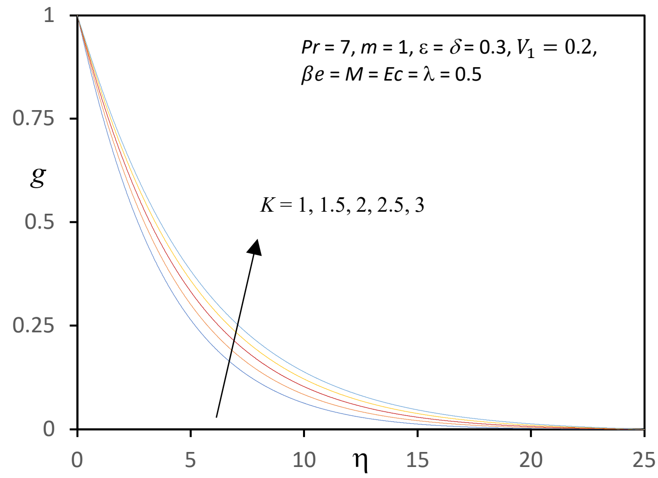

Fig. 9. Influence of K on tangential velocity profiles.

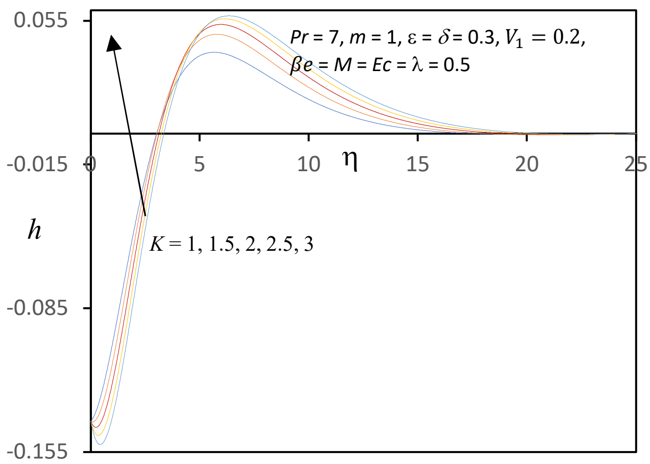

Fig. 10. Influence of K on angular velocity profiles.

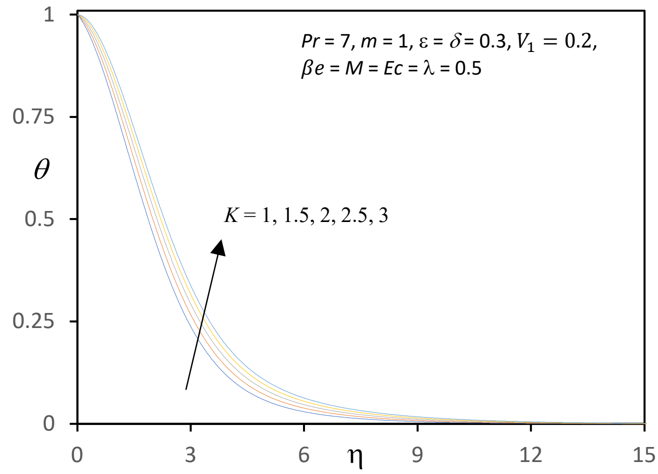

Fig. 11. Influence of K on temperature profiles.

Figure 6 illustrates that micro-rotation (angular velocity), h, undergoes a much more complex response to a variation in first Eyring-Powell rheological parameter, ε. Initially near the cone surface, a significant reduction in micro-rotation is produced with larger values of ε. This parameter does not feature directly in the Eringen micro-rotation Eq. (21); however, it is strongly coupled to both the axial and tangential linear momentum boundary layer Eqs. (19) and (20) in multiple terms. Further from the wall the reverse effect is computed- micro-element angular velocities are significantly boosted with increasing first Eyring-Powell rheological parameter, ε since greater space is present for the micro-elements to spin further from the wall. However, the magnitudes are lower than near the cone surface where space is constrained, and this impedes gyratory motions. There is clearly a non-trivial influence of the magnetic polymer viscosity via the Eyring-Powell characteristics on micropolar rheology. Spin of the micro-elements is influenced differently depending on the location from the cone surface as reflected in the point of inflection in the graph. Near the wall the reverse spin is induced whereas further from the wall positive spin is sustained at all values of ε. Again, excellent convergence of the Keller box code is achieved in the smooth profiles in the free stream (edge of the boundary layer) confirming that a sufficiently large infinity boundary condition has been correctly deployed in the computations.

Figure 7 reveals that a consistent enhancement in temperature is produced and a corresponding increase in thermal boundary layer thickness, with an increment in the first Eyring-Powell rheological parameter, ε. This trend is sustained at all locations from the cone surface (wall) to the free stream. In all cases, peak temperature is computed at the wall and descends monotonically into the freestream.

Figures 8 to 11 illustrates the effect of the Eringen number i.e., coupling parameter *K*, on the axial velocity (f'), tangential velocity (*g*), angular velocity (*h*) and temperature (θ), distributions through the boundary layer regime. This key micropolar parameter, $K = k/\mu$ defines the ratio of Eringen vortex viscosity to Newtonian dynamic viscosity. It features only in the augmented axial shear term, $\Pr(1+K+\varepsilon)f'''$ in Eq. (19) and the micropolar coupling term, $+Kh'$ which links the axial momentum Eq. (19) directly to the angular momentum Eq. (21). As $K \to 0$, gyratory motions of micro-elements vanish, and the magnetic polymer is described solely by the Eyring-Powell model. When $K = 1$, both micropolar vortex viscosity and dynamic viscosity are equal. With increment in *K*, the micropolar vortex viscosity begins to dominate. Figure 8 shows that near the cone surface; this generates an assistive effect leading to weak acceleration in the axial flow. At greater distance from the wall, the reverse influence is computed with strong deceleration and a decrease in momentum boundary-layer thickness. Very weak reverse axial flow is only computed close to the free stream.

Figure 9 demonstrates that a consistent enhancement in tangential velocity accompanies an increase in *K* values. Therefore, while strongly micropolar liquids decelerate the axial flow, they accelerate tangential flow. A similar result has been observed in Eldahab and Elaziz [51] although in the absence of Eyring-Powell non-Newtonian effects.

Figure 10 indicates that in the vicinity of the cone surface $(\eta = 0)$ the reverse spin of micro-elements (negative micro-rotation) is suppressed with greater *K* values. Further from the cone surface, however, after maximum micro-rotation magnitudes (positive spin) are attained *the contrary behavior is observed and retardation in spin of micro-elements is induced, with a strong decrement in micro-rotation accompanying an increase in K*. The micro-rotation peak also migrates closer to the wall (cone surface) as *K* values increase.

Figure 11 shows that with elevation in *K* values there is a substantial boost in temperature magnitudes. Stronger micropolar fluids therefore heat the regime and enhance thermal boundary layer thickness compared with weak micropolar fluids (lower *K* values). Figures 12 to 14 illustrates the effect of the s*urface temperature exponent m*, on the axial velocity (f'), angular velocity (*h*) and temperature (θ) distributions through the boundary layer regime. The non-isothermal power-law index, *m*, arises in many terms in all the boundary layer equations. For example, it appears in the convective nonlinear terms, $\xi(1-\xi)((1-m)/4)\times (f'.\partial f'/\partial\xi - f''.\partial f/\partial\xi)$ in the axial momentum Eq. (19). For the case *m* = 0 the cone surface becomes isothermal. As *m* is increased (Fig. 12) the axial velocity is strongly depleted throughout the boundary layer. Figure 13 is also suppressed although in this case negative values are computed close to the cone surface (flow reversal i.e., reverse spin of micro-elements). In the case of the axial flow, no flow reversal is observed. Figure 14 indicates that temperature is also reduced strongly with increasing non-isothermal power-law index, *m*. Thermal boundary layer thickness is therefore also decreased.

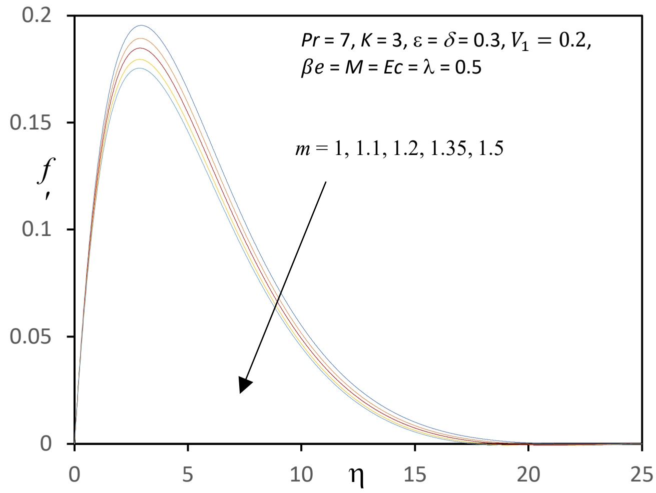

Fig. 12. Influence of *m* on axial velocity profiles.

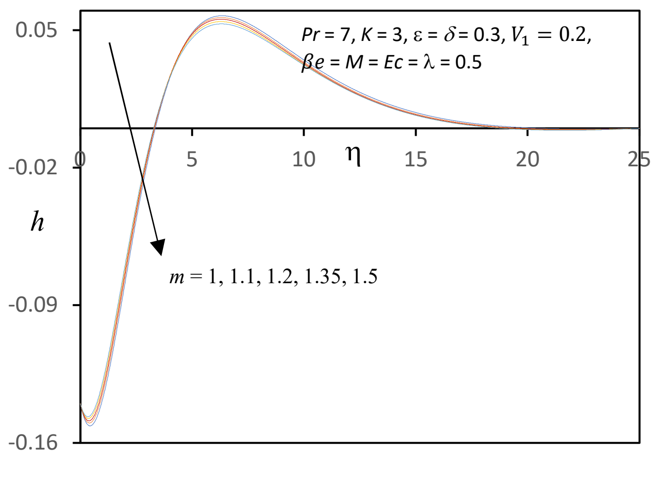

Fig. 13. Influence of *m* on angular velocity profiles.

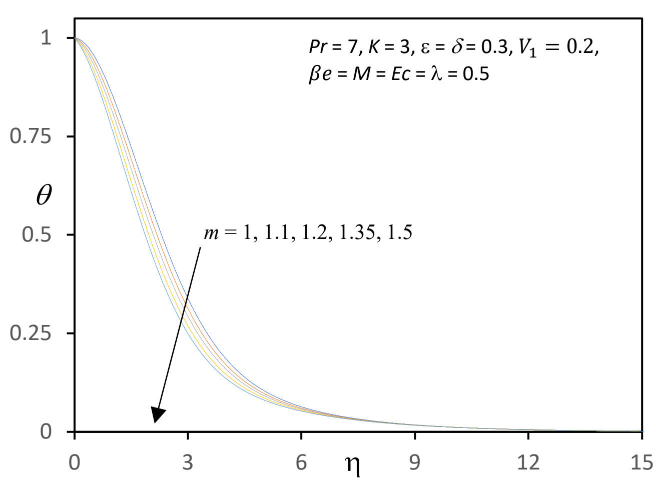

Fig. 14. Influence of *m* on temperature profiles.

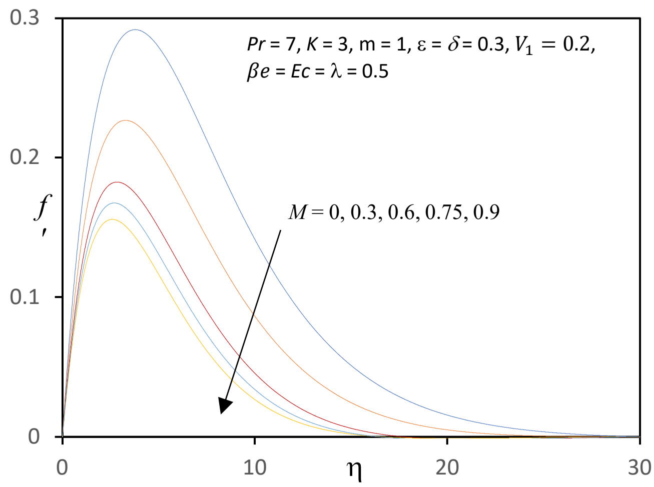

Fig. 15. Influence of *M* on axial velocity profiles.

Figures 15 to 18 illustrates the effect of the *magnetic interaction parameter* M, on the axial velocity (f'), tangential velocity (g), angular velocity (h) and temperature (θ) distributions through the boundary layer regime. The parameter $M = \sigma B_0^2 / \rho\Omega \sin\varphi$ relates the ratio of Lorentzian magnetic drag force to the centrifugal inertial force in the regime. It arises in three of the four boundary layer equations. Firstly, in the axial momentum Eq. (19) in the term, $-\mathrm{Pr}\,M\xi^2(f'+\beta_e \mathrm{Pr}\,\xi^2 g)/(1+\beta_e^2)$. Secondly in the tangential momentum Eq. (20), $M(\beta_e f'-\mathrm{Pr}\,\xi^2 g)/(1+\beta_e^2)$. Thirdly, it features in the Ohmic heating (Joule magnetic dissipation) term in the thermal boundary layer eqn. (22). For the case M = 0 magnetic field vanishes. Figure 15 reveals that with increment in M (stronger magnetic field), the axial velocity is damped strongly.

Similarly with larger values of M, the tangential velocity is also suppressed in Fig. 16. Stronger magnetic field therefore for Eyring-Powell micropolar magnetized polymers produces both axial and tangential flow deceleration. In both these figures, these patterns are sustained from the cone surface to the free stream. Momentum boundary layer thickness is therefore elevated.

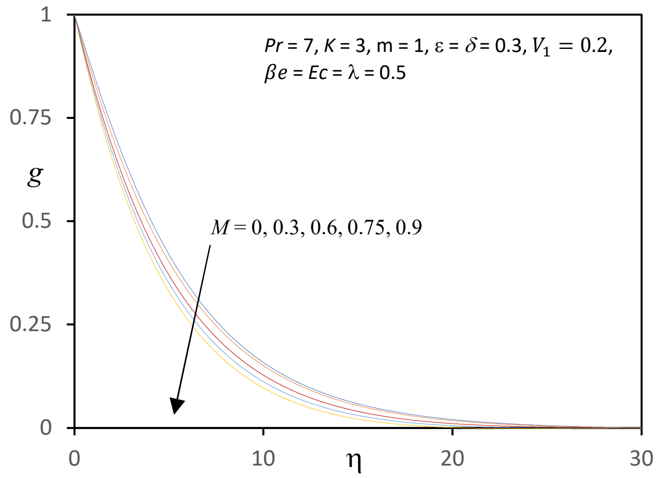

Fig. 16. Influence of M on tangential velocity profiles.

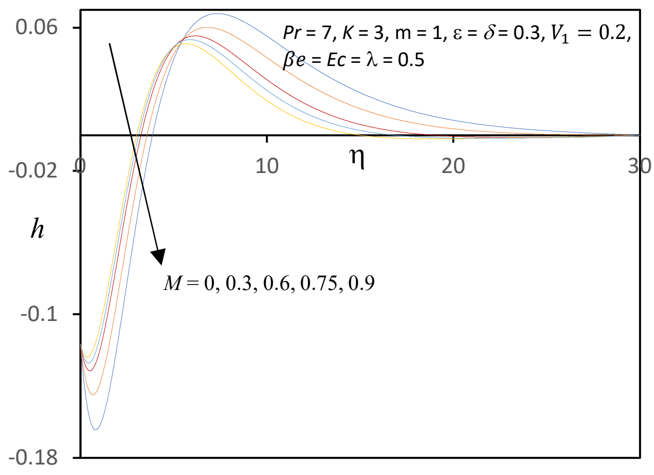

Fig. 17. Influence of M on angular velocity profiles.

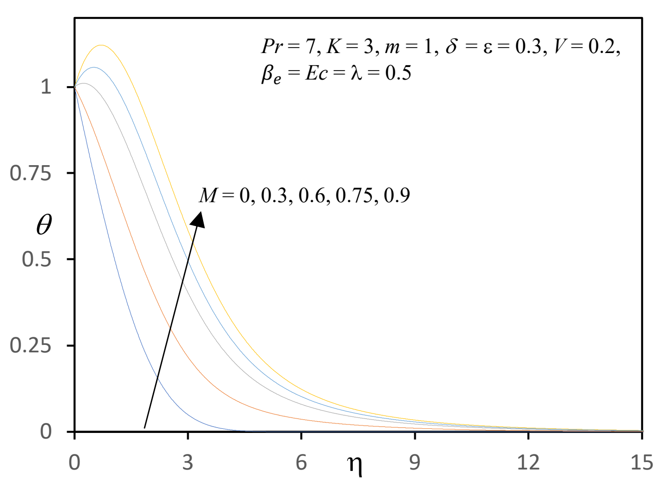

Fig. 18. Influence of M on temperature profiles.

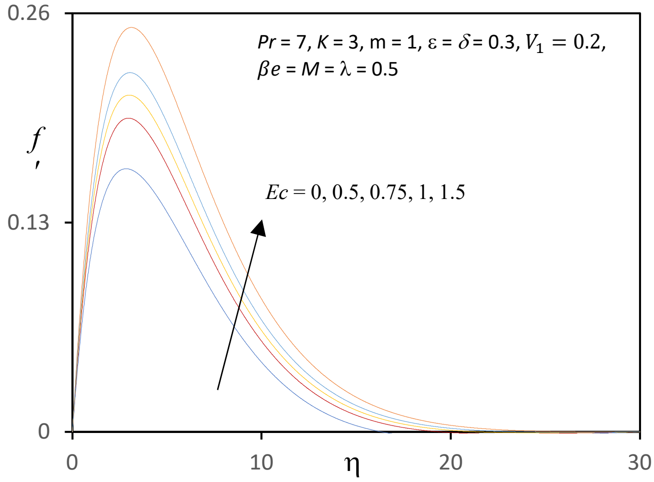

Fig. 19. Influence of Ec on axial velocity profiles.

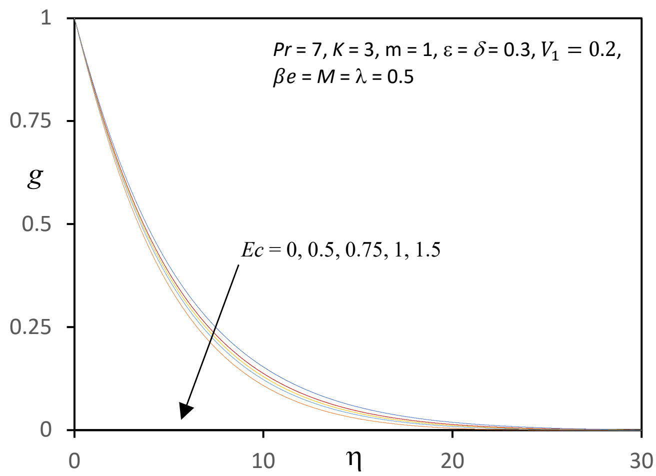

Fig. 20. Influence of Ec on tangential velocity profiles.

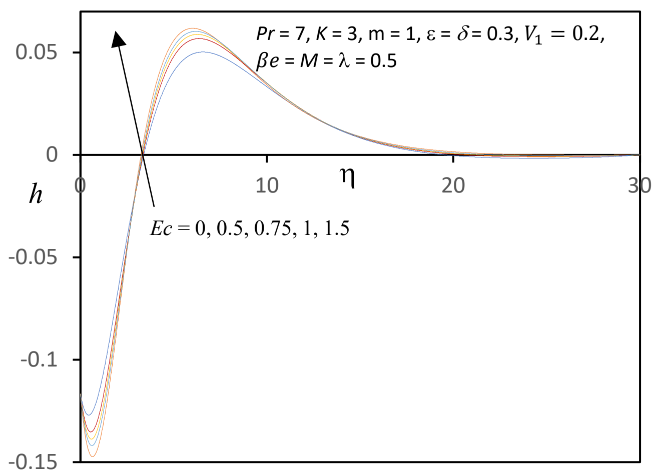

Fig. 21. Influence of Ec on angular velocity profiles.

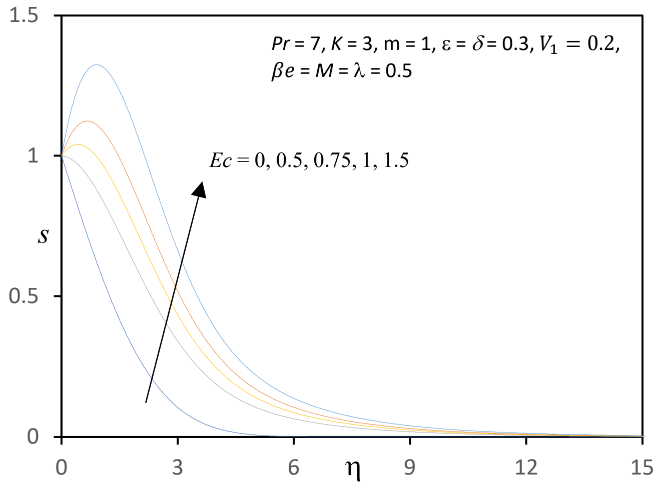

Fig. 22. Influence of *Ec* on temperature profiles.

Figure 17 indicates that close to the wall (cone surface) there is a suppression in micro-rotation (angular velocity) but further from the wall, strong acceleration in micro-element spin is generated (angular velocities are increased). Figure 18 shows that temperature is significantly enhanced with an increase in magnetic interaction parameter, *M*. For *M* = 0, 0.3 no temperature overshoot is computed although an overshoot does arise for *M* > 0.3. The excess work expended in dragging the magnetic polymer against the action of the radial magnetic field generates heat which elevates temperatures. Elevation in magnetic field strength effectively heats the boundary layer regime and increases thermal boundary layer on the cone surface.

Figures 19 to 22 illustrates the effect of the *Eckert number* (*Ec*), on the axial velocity (f'), tangential velocity (*g*), angular velocity (*h*) and temperature (θ) distributions through the boundary layer regime. *Ec* simulates the relative contribution of kinetic energy dissipated as internal friction to the boundary layer enthalpy difference. It is generated by molecular ballistic collisions in the magnetic polymer due to internal friction which creates a heating effect. *Ec* also contributes to the Ohmic heating term, which describes resistance to electrical current by the magnetic polymer and is also known as Joule heating. These two terms appear in the thermal boundary layer Eq. (16) as $Ec M(f'^2 + \Pr^2 \xi^4 g^2)/(1+\beta_e^2)$ and clearly couple both the axial velocity and the tangential velocity fields. Figure 19 shows that axial velocity is strongly boosted with Eckert number whereas Fig. 20 shows that tangential velocity is suppressed. For the case, *Ec* = 0 both viscous and Joule (Ohmic) dissipation vanish.

Figure 21 indicates that with increment in Eckert number, there is strong elevation in micro-rotation. Viscous and Joule heating therefore encourages the intensity of gyratory motions of microelements in the boundary layer. Finally, Fig. 22 shows that as Eckert number is increased, there is a significant enhancement in temperatures. The dissipation generates strong heating via kinetic energy dissipation which elevates thermal boundary layer thickness on the cone surface.

Table 2 presents the Keller box numerical solutions for the impact of the Eyring-Powell second *non-Newtonian parameter* (δ), material parameter (V_1), Prandtl number (*Pr*), material parameter (λ), *Eyring-Powell second rheological fluid parameter* (ε), *Hall parameter* (β_e) and stream wise coordinate value, ξ on local skin frictions (C_{fx} and C_{gx}), wall couple stress (*Wcs*) and Nusselt number i.e. wall heat transfer rate (*Nu*). Solutions are given both at cone vertex point ($\xi = 0$) and at a general point along the cone slant length ($\xi = 1$). With increasing second Eyring-Powell rheological parameter (δ), for $\xi = 0$, axial skin friction (C_{fx}) is suppressed whereas no values are computed for tangential skin friction (C_{gx}), and a slight increase is observed in wall couple stress (*Wcs*) and Nusselt number (*Nu*). With an increase in streamwise coordinate, to $\xi = 1$, *a* significant elevation is observed in axial skin friction (C_{fx}) whereas tangential skin friction (C_{gx}), wall couple stress (*Wcs*) and Nusselt number (*Nu*) are all strongly reduced.

An increase in spin gradient viscosity parameter (V_1) generally decreases local skin frictions (C_{fx} and C_{gx}), wall couple stress (*Wcs*) but weakly enhances Nusselt number (*Nu*), at both streamwise coordinate values ($\xi = 0,1$). An increment in Prandtl number produces at the cone vertex, an increase in C_{fx}, no change in the vanishing value of zero for C_{gx} and a reduction in both *Wcs* and *Nu; at* $\xi = 1$, *the same trends are observed for* C_{fx}, *Wcs*, *Nu but additionally a decrement is also computed in tangential skin friction*, C_{gx}.

With increasing values of λ i.e., the dimensionless Eringen spin gradient viscosity, C_{fx} *and Wcs are both enhanced whereas Nu* values are suppressed; however, there is not alteration in the tangential skin friction which remains zero at the cone vertex, $\xi = 0$. Further along the cone surface from the vertex, at $\xi = 1$, local axial skin friction (C_{fx}) is increased again as are tangential skin friction C_{gx} and wall couple stress (*Wcs*) – however negative values are computed for C_{gx} and *Wcs*.

There is also a strong reduction in Nusselt number (*Nu*). Higher values of the parameter $\lambda = \gamma / j\mu$ therefor exert a strong influence on all wall characteristics indicating that spin gradient viscosity, micro-inertia per unit mass and dynamic viscosity all contribute to the modifications as embodied in this parameter. With elevation in the first Eyring-Powell rheological parameter (ε), local axial skin friction (C_{fx}), wall couple stress (*Wcs*) and Nusselt number (*Nu*) are all enhanced whereas no effect is computed again on tangential skin friction, C_{gx} at the cone vertex, $\xi = 0$. At $\xi = 1$, local axial skin friction (C_{fx}) and wall couple stress (*Wcs*) are both increased whereas tangential skin friction, C_{gx}, and Nusselt number (*Nu*) are depleted.

Finally, the impact of Hall current β_e, on local skin frictions (C_{fx} and C_{gx}), wall couple stress (*Wcs*) and Nusselt number i.e. wall heat transfer rate (*Nu*) is documented. The parameter β_e arises in $-\Pr M \xi^2 (f' + \beta_e \Pr \xi^2 g)/(1+\beta_e^2)$ in the Eq. (19), $M(\beta_e f' - \Pr \xi^2 g)/(1+\beta_e^2)$ in Eq. (20) and the combined viscous heating/Joule dissipation terms, $Ec M(f'^2 + \Pr^2 \xi^4 g^2)/(1+\beta_e^2)$ in the energy Eq. (22). It does not arise in the micro-rotation equation (21), although coupling via other equations, it does influence the angular velocity. Hall current parameter always arises as an inverse squared term and is responsible for the crossflow nature of the magnetic field (it is orientated perpendicularly to the applied magnetic field). The Hall parameter is also coupled with the magnetic interaction parameter, *M*. The Hall current effect quantifies the charge separation phenomenon in the electro-conductive polymer as it swirls around the cone in the magnetic field. This charge separation is produced by the opposing Lorentz forces on the positive and negative charges, and leads to an externally measurable voltage, termed the Hall voltage. The Hall voltage amplitude is controlled effectively by the strength of the Lorentz force and the charge density and mobility.

Table 2. Variation in of C_{fx}, C_{gx}, Wcs and Nu for different values of ε, δ, Pr, V_1, λ, β_e, ξ.

δ	V_1	Pr	λ	ε	β_e	$\xi = 0.0$				$\xi = 1.0$			
						C_{fx}	C_{gx}	Wcs	Nu	C_{fx}	C_{gx}	Wcs	Nu
0						0.7306	0	0.9010	0.5136	3.3950	-1.0746	-56.859	-5.9966
0.1						0.7295	0	0.9010	0.5136	3.2946	-1.5228	-56.841	-5.9856
0.2						0.7279	0	0.9011	0.5137	3.1378	-2.2327	-56.769	-5.9669
0.3						0.7268	0	0.9011	0.5137	3.0290	-2.7451	-56.676	-5.9523
0.4						0.7251	0	0.9012	0.5138	2.8590	-3.6353	-56.423	-5.9241
	0					0.3160	0	0.7145	0.4078	3.2687	-1.7339	1.4932	-6.1157
	0.2					0.3156	0	0.0940	0.4097	3.2031	-1.7667	-119.68	-5.901
	0.4					0.3150	0	-0.5803	0.4110	3.1693	-1.7833	-197.39	-5.841
	1					0.3146	0	-1.2415	0.4121	3.1507	-1.7862	-259.27	-5.7977
	2					0.3135	0	-1.9341	0.4131	3.1377	-1.7900	-312.25	-5.7567
		5				0.4030	0	0.1078	0.5176	2.3935	-1.4288	-42.750	-2.9558
		6				0.4060	0	0.1077	0.5152	2.7879	-1.5822	-74.743	-4.3298
		7				0.4163	0	0.0940	0.5137	3.2031	-1.7667	-119.68	-5.9009
		8				0.4274	0	0.0650	0.5119	3.6008	-1.9840	-179.74	-7.6585
		10				0.4514	0	-0.0458	0.5097	4.3319	-2.5293	-353.87	-11.698
			0.01			0.7252	0	0.4868	0.4125	3.1191	-1.7913	-807.66	-5.7241
			0.1			0.7271	0	0.6689	0.4094	3.1869	-1.7699	-192.11	-5.8648
			0.5			0.7290	0	0.9010	0.4086	3.2432	-1.7536	-56.824	-5.9797
			1			0.7335	0	1.7053	0.4082	3.2616	-1.7479	-30.851	-6.0185
			2			0.7389	0	3.9393	0.4075	3.2735	-1.7437	-15.637	-6.0475
				0		0.6844	0	0.4778	0.522	3.1414	-0.996	-57.94	-5.851
				0.5		0.7568	0	0.4792	0.508	3.3186	-2.226	-56.12	-6.061
				1		0.8204	0	0.4809	0.496	3.5263	-3.295	-54.43	-6.260
				1.5		0.8770	0	0.4826	0.485	3.7537	-4.236	-52.91	-6.444
				2		0.9280	0	0.4844	0.476	3.9924	-5.063	-51.55	-6.619
					0.1	0.7358	0	0.8920	0.4078	3.6933	-2.0868	-141.58	-6.6899
					0.25	0.7340	0	0.8980	0.4083	3.4504	-1.9756	-130.16	-6.6217
					0.5	0.7290	0	0.9010	0.4100	3.2031	-1.7667	-126.78	-5.9009
					0.65	0.7257	0	0.9056	0.4106	3.1584	-1.6503	-119.68	-5.2303
					1	0.7192	0	0.9072	0.4126	3.2639	-1.4488	-118.66	-3.5428

Table 3. Variation in C_{fx}, C_{gx}, Wcs and Nu for different values of K, m, M, Ec and ξ.

K	m	M	Ec	$\xi = 0.0$				$\xi = 1.0$			
				C_{fx}	C_{gx}	Wcs	Nu	C_{fx}	C_{gx}	Wcs	Nu
1				0.7290	0	0.9010	0.5858	2.6261	-2.4564	-30.807	-4.8492
1.5				0.7324	0	0.8321	0.5622	2.8185	-2.0938	-51.499	-5.1933
2				0.7375	0	0.7616	0.5432	2.9664	-1.9281	-73.425	-5.4716
2.5				0.7456	0	0.6892	0.5273	3.0923	-1.8280	-96.293	-5.6994
3				0.7588	0	0.6147	0.5137	3.2031	-1.7667	-119.68	-5.9009
	1			0.7290	0	0.9010	0.5137	3.2432	-1.7536	-56.824	-57.391
	1.1			0.7206	0	0.9053	0.5216	3.1908	-1.7643	-54.770	-9.5947
	1.2			0.7127	0	0.9096	0.5293	3.1578	-1.7607	-53.414	-5.9797
	1.35			0.7016	0	0.9159	0.5402	3.1094	-1.7617	-51.928	-5.5589
	1.5			0.6913	0	0.9222	0.5505	3.0748	-1.7635	-50.085	-4.9021
		0		0.7542	0	0.8787	0.5170	4.8778	-1.3661	-108.26	1.1041
		0.3		0.7440	0	0.8915	0.5151	3.9252	-1.5694	-76.695	-2.9554
		0.6		0.7347	0	0.9062	0.5129	2.9044	-1.8570	-47.484	-7.6343
		0.75		0.7186	0	0.9146	0.5116	2.4117	-2.0258	-34.453	-10.426
		0.9		0.7052	0	0.9230	0.5101	1.9552	-2.2137	-22.978	-12.243
			0	0.7052	0	0.8787	0.5170	3.2411	-1.7175	-56.785	0.8884
			0.5	0.7290	0	0.9010	0.5137	3.2432	-1.7536	-56.824	-5.9797
			0.75	0.7440	0	0.9143	0.5116	3.2458	-1.7589	-56.871	-9.4108
			1	0.7616	0	0.9291	0.5091	3.2494	-1.7660	-56.940	-12.839
			1.5	0.8148	0	0.8035	0.5011	3.2685	-1.790	-57.845	-19.709

It can be significant in spin coating operations. Hall voltage is directly proportional to the product of electrical conductivity and axial magnetic field. The case of $\beta_e \to 0$ corresponds to vanishing Hall current. At the cone vertex $(\xi = 0)$ increasing Hall current parameter does not influence the tangential skin friction, C_{gx} (which as noted before does not exist here) but decreases axial skin friction (C_{fx}); however, it strongly elevates the wall couple stress (Wcs) and Nusselt number (Nu). At $\xi = 1$, *again greater values of Hall parameter reduce the* axial skin friction (C_{fx}) but elevate tangential skin friction, C_{gx}, wall couple stress (Wcs) and Nusselt number (Nu) - i.e., values become less negative.

Table 3 gives the Keller box solutions for the influence of *Eringen number* (K), *magnetic interaction parameter* (M), *surface temperature exponent* i.e., *non-isothermal power-law index* (m), *Eckert number* (Ec) *and traverse coordinate* (ξ) on local skin frictions (C_{fx} and C_{gx}), wall couple stress (Wcs) and heat transfer rate (Nu) at the cone surface.

Elevation in K values, at the cone vertex $(\xi = 0)$, local axial skin friction (C_{fx}) is boosted whereas wall couple stress (Wcs) and Nusselt number (Nu) are both suppressed. Further along the cone surface from the vertex, at $\xi = 1$, both axial skin friction (C_{fx}) and tangential skin friction, C_{gx} are enhanced and once again both wall couple stress (Wcs) and Nusselt number (Nu) are very markedly reduced.

With increment in non-isothermal power-law index (m), axial skin friction (C_{fx}) is reduced at the cone vertex $(\xi = 0)$, no change arises in tangential skin friction, C_{gx}, and both wall couple stress (Wcs) and Nusselt number (Nu) are elevated. Further along the wall (cone surface) from the vertex, at $\xi = 1$, *both axial and tangential skin friction are reduced whereas again* both wall couple stress (Wcs) and Nusselt number (Nu) are boosted.

With the increasing magnetic interaction parameter (M), at the cone vertex the tangential skin friction is unchanged whereas it is strongly decreased further along the wall $\xi = 1$; axial skin friction and Nusselt number are suppressed at both locations whereas wall couple stress (Wcs) is considerably enhanced.

Finally, an increase in Eckert number (which ramps up both the viscous and Ohmic heating), produces a strong increase in axial skin friction at both the cone vertex and further along the cone wall, whereas it has no effect on the tangential skin friction at the cone vertex but does induce a considerable reduction further along the cone surface. Wall couple stress i.e., micro-rotation gradient at the wall, (Wcs) and Nusselt number (Nu) are both substantially depleted with increasing Eckert number at both stations considered for the streamwise coordinate (ξ).

5. Conclusions

Numerical solutions have been presented for the non-similar, incompressible steady state laminar convective boundary layer flow of an Eyring-Powell-Eringen micropolar magnetic polymer external to a rotating vertical non-isothermal cone, as a simulating of swirl functional rheological film coating dynamics. The Keller-box implicit second order accurate finite difference numerical scheme has been utilized to efficiently solve the transformed, dimensionless linear and angular momentum and thermal boundary layer equations, subject to realistic boundary conditions. A comprehensive assessment of the effects of Eyring first and second rheological fluid parameters (ε, δ), non-isothermal power-law index i.e. surface temperature exponent (m), Prandtl number (Pr), magnetic interaction parameter (M), Hall current parameter (β_e), Eckert number (Ec), micropolar fluid material parameters (V_1, λ), and Eringen number *(vortex viscosity parameter)* (K) on thermo-fluid characteristics has been conducted. Excellent correlation with previous studies has been demonstrated testifying to the validity of the present code. The present computations have shown that:

(i) Increase in ε produces a significant deceleration in the axial flow which is sustained into the freestream. Strong tangential flow acceleration is computed throughout the boundary layer regime from the wall to the freestream with elevation in ε. Micro-rotation (angular velocity) is significantly boosted with increasing ε. A strong elevation in temperature and thermal boundary layer thickness is induced with increasing ε.

(ii) With greater K, a strong axial deceleration is computed, whereas tangential flow acceleration is observed. A reverse spin of micro-elements is suppressed with greater K values. Also, with elevation in K values there is a considerable increase in temperature.

(iii) As m is increased, a strong axial flow deceleration and damping in angular velocity is computed and also there is a considerable depletion in temperature.

(iv) With an increment in M both axial and tangential flow deceleration is produced whereas there is a strong enhancement in micro-rotation and temperature is markedly accentuated.

(v) Increasing Ec is observed to boost axial velocity, temperature and micro-rotation but suppresses the tangential velocity.

(vi) With increasing λ values, C_{fx}, C_{gx} and Wcs is elevated whereas there is a strong reduction in Nu.

(vii) Increasing β_e does not modify C_{gx} whereas it strongly decreases C_{fx} but elevates the Wcs and Nu.

(viii) With increasing δ, at the cone vertex $\xi = 0$, C_{fx} is suppressed, and a slight increase is observed in Wcs and Nu. With an increase in streamwise coordinate, to $\xi = 1$, *a* significant elevation is observed in C_{fx} whereas C_{gx}, Wcs and Nu are strongly reduced.

(ix) An increase in V_1 decreases C_{fx}, C_{gx} and Wcs but weakly enhances Nu, at both $\xi = 0$, and 1.

(x) An increment in Pr at $\xi = 0$, produces an increase in C_{fx}, and a reduction in both Wcs and Nu; *at* $\xi = 1$, *the same trends are observed for* C_{fx}, Wcs, Nu but additionally a strong depletion is computed in C_{gx}.

Generally, very stable and accurate solutions have been obtained with the present finite difference code. The numerical code is able to solve nonlinear boundary layer equations very efficiently and therefore shows excellent promise in simulating transport phenomena in other non-Newtonian fluids. Some limitations of the study are, however, the absence of time-dependence and non-Fourier heat conduction effects. Future studies will address these aspects and also alternative non-Newtonian models e.g., viscoplastic (yield stress) fluids which also characterize magnetic polymers.

Author Contributions

S. Abdul Gaffar planned the scheme, design, material preparation, data collection and analysis; O. Anwar Bég, T.A. Bég, S. Kuharat and P. Ramesh Reddy wrote the first draft and revised the manuscript. The manuscript was written through the contribution of all authors. All authors discussed the results, reviewed, and approved the final version of the manuscript.

Acknowledgments

We express our deepest gratitude and appreciation for the assistance and support received throughout the completion of this research paper from our co-authors. We want to take this opportunity to acknowledge the contributions of the individuals who played a significant role in successfully completing this research.

Conflict of Interest

The authors declared no potential conflicts of interest concerning the research, authorship, and publication of this article.

Funding

The authors received no financial support for the research, authorship, and publication of this article.

Data Availability Statements

The datasets generated and/or analyzed during the current study are available from the corresponding author on reasonable request.

Nomenclature

B	Material parameter (Tesla)
B_0	Constant imposed magnetic field (Tesla)
C	Rheological fluid parameter
C_{fs}	Skin friction coefficient
c_p	Specific heat (J/kgK)
e	Electron charge (Coulombs)
Ec	Eckert number
$\boldsymbol{f}$	Body force per unit mass vector (N/kg)
f	Non-dimensional stream function
g	Eringen's micro-rotation (angular velocity) (s^{-1})
g_1	Acceleration due to gravity (m/s^2)
Gr_x	Local Grashof number
$\boldsymbol{h}$	Angular velocity (microrotation or gyration) vector (rad/s)
j	Microinertia per unit mass (kg·m^2)
k	Vortex viscosity (Pa. s)
K	Micropolar coupling parameter (ratio of micropolar and dynamic viscosities)
$\boldsymbol{l}$	Body couple per unit mass vector (N.m/kg)
m	Surface temperature exponent
M	Magnetic parameter (Tesla)
m_e	Mass Electron (kg)
N	Microrotation component (s^{-1})
n_e	Electron number density
Nu	Heat transfer rate (Local Nusselt number)
Pr	Prandtl number
r	Local radius of the cone
Re	Local rotational Reynolds number
Ra	Local Rayleigh number
T	Temperature of the fluid (Kelvins)
t_e	Electron collision time
u, v, w	Non-dimensional velocity components along the x, y, z directions, respectively, (m/s)
$\mathbf{V}$	Translational velocity vector
V	Velocity vector (m/s)
V_1	Micropolar spin gradient viscosity material parameter (kg.m/s)
Wcs	Wall couple stress (N/m^2)
x	Stream wise coordinate (m)
y	Transverse coordinate (m)
Greek	
φ	Half angle of the cone (Radian)
α	Thermal diffusivity (m^2/s)
β_1	Coefficient of thermal expansion (/K)
μ	Dynamic viscosity (kg m/s)
ν	Kinematic viscosity (m^2/s)
ρ	Density of non-Newtonian fluid (kg/m^3)
γ	Eringen's spin gradient viscosity (kg m s^{-1})
$\omega_e(= eB_0/m_e)$	Electron frequency (rad·s^{-1})
$\sigma(= e^2 n_e t_e/m_e)$	Electrical conductivity (Siemens/m)
β	Eyring-Powell fluid parameter
ε	Eyring-Powell first rheological fluid parameter
δ	Eyring-Powell second non-Newtonian parameter
η	Dimensionless radial coordinate
θ	Non-dimensional temperature
ξ	The dimensionless tangential coordinate
ψ	Dimensionless stream function
Ω	Eringen's micro-rotation (angular velocity)
λ	Eringen second order viscosity coefficient
$\beta_e = (\omega_e \tau_e)$	Hall current parameter
$\alpha^*, \beta^*, \gamma$	Spin gradient viscosity coefficients for micropolar fluids
Subscripts	
w	Conditions at the wall (cone surface)
∞	Free stream conditions

References

[1] Rangappa, S.M., Kumar, J., Pillai, P., Siengchin, S., *Polymer Coatings: Technologies and Applications*, 379 pp, CRC Press, Florida, USA, 2022.
[2] Goddard, J.D., Polymer Fluid Mechanics, *Advances in Applied Mechanics*, 19, 1979, 143-219.
[3] Bird, R.B., Giacomin, A.J., Polymer fluid dynamics: Continuum and Molecular Approaches, *Annual Review of Chemical and Biomolecular Engineering*, 7, 2016, 479-507.
[4] Kistler, S.F., The fluid mechanics of curtain coating and related viscous surface flows with contact lines, *Ph.D. Thesis, University of Minnesota-Minneapolis*, USA, 1983.
[5] Ali, N., Zaman, A., Anwar Bég, O., Hayat, T., Mathematical model for isothermal wire-coating from a bath of Giesekus viscoelastic fluid, *Chemical Engineering Communications* 203, 2016, 1336-1248.
[6] Bajaj, M., Ravi Prakash, J., Pasquali, M., A computational study of the effect of viscoelasticity on slot coating flow of dilute polymer solutions, *Journal of Non-Newtonian Fluid Mechanics,* 149, 2008, 104–123.
[7] Norouzi, M., Daghighi, S.Z., Anwar Bég, O., Exact analysis of heat convection of viscoelastic FENE-P fluids through isothermal slits and tubes, *Meccanica,* 53, 2018, 817-831.
[8] Zafar, M., Rana, M.A., Zahid, M., Ahmad, B., Mathematical Analysis of the coating process over a porous web lubricated with upper-convected Maxwell fluid, *Coatings*, 9(7), 2019, 458.
[9] Yoon H.K., Ghajar, A.J., A note on the Powell-Eyring fluid model, *International Communications in Heat and Mass Transfer*, 14, 1987, 381-390.
[10] Hayat, T., Khan, M.W.A., Alsaedi, A., Ayub, M., Khan, M.I., Stretched flow of Oldroyd-B fluid with Cattaneo-Christov heat flux, *Results in Physics*, 7, 2017, 2470–2476.
[11] Sharma, R.P., Shaw, S., MHD Non-Newtonian Fluid Flow past a Stretching Sheet under the Influence of Non-linear Radiation and Viscous Dissipation, *Journal of Applied and Computational Mechanics*, 8(3), 2022, 949-961.
[12] Hassan, M., Ahsan, M., Usman, Alghamdi, M., Muhammad, T., Entropy generation and flow characteristics of Powell Eyring fluid under effects of time sale and viscosities parameters, *Scientific Reports*, 13, 2023, 8376.
[13] Rosca A.V., Pop, I., Flow and heat transfer of Powell–Eyring fluid over a shrinking surface in a parallel free stream, *International Journal of Heat and Mass Transfer*, 71, 2014, 321-327.
[14] Jalil, M., Asghar, S., Imran, S.M., Self-similar solutions for the flow and heat transfer of Powell–Eyring fluid over a moving surface in a parallel free stream, *International Journal of Heat and Mass Transfer*, 65, 2013, 73-79.

[15] Aatif, M., Waqas, M., Anwar Bég, O., Zubair, M., Khan W.A., Kadir, A., Computation of Sakiadis flow of an Eyring-Powell rheological fluid from a moving porous surface with a non-Fourier heat flux model, *Waves in Random and Complex Media,* 35(7), 2026, 14351 – 14369.
[16] Khan, I., Khan, M.W.A., Computational analysis of hybrid nanoparticles dispersion in Powell-Eyring fluid flow over a stretching surface: A comparative simulation study, *Alexandria Engineering Journal*, 93, 2024, 328–335.
[17] Abdelmalek, Z., Khan, I., Khan, M.W.A., Rehman, K.U., Sherif, E.S.M., Computational analysis of nano-fluid due to a non-linear variable thicked stretching sheet subjected to Joule heating and thermal radiation, *Journal of Materials Research and Technology,* 9(5), 2020, 11035–11044.
[18] Ivan Novikau, S., Vladimir Zverev, S., Ekaterina Novak, V., Sofia Kantorovich, S., Stockmayer supra-colloidal magnetic polymers under the influence of an applied magnetic field and a shear flow, *Journal of Molecular Liquids,* 384, 2023, 122229.
[19] Lopez-Lopez, M.T., Durán, J.D., Iskakova, L.Y., Zubarev, A.Y., Mechanics of Magnetopolymer composites: A Review, *Journal of Nanofluids*, 5(4), 2016, 479–495.
[20] Kumaran, G., Sivaraj, R., Ramachandra Prasad, V., Anwar Bég, O., Prakash Sharma, R., Finite difference computation of free magneto-convective Powell-Eyring nanofluid flow over a permeable cylinder with variable thermal conductivity, *Physica Scripta,* 96(2), 2021, 025222.
[21] Khan, Z., Rasheed, H.U., Abbas, T., Khan, W., Khan, I., Baleanu, D., Sooppy Nisar, K., Analysis of Eyring–Powell Fluid Flow Used as a Coating Material for Wire with Variable Viscosity Effect along with Thermal Radiation and Joule Heating, *Crystals*, 10(3), 2020, 168.
[22] Satya Narayana, P.V., Tarakaramu, N., Moliya Akshit, S., Ghori, J.P., MHD flow and heat transfer of an Eyring – Powell fluid over a linear stretching sheet with viscous dissipation - A Numerical Study, *Frontiers in Heat and Mass Transfer*, 9(1), 2017, 1-5.
[23] Parmar, A., Jain, S., MHD Powell-Eyring fluid flow with non-linear radiation and variable thermal conductivity over a permeable cylinder, *International Journal of Heat and Technology*, 36, 2018, 56–64.
[24] Khan, N.A., Sultan, F., Khan, N.A., Heat and Mass Transfer of Thermophoretic MHD Flow of Powell–Eyring Fluid over a Vertical Stretching Sheet in the Presence of Chemical Reaction and Joule Heating, *International Journal of Chemical Reactor Engineering*, 13(1), 2015, 37-49.
[25] Eringen, A.C., Theory of micropolar fluids, *Journal of Mathematics and Mechanics,* 16(1), 1966, 1-18.
[26] Lukaszewicz, G., *Micropolar fluids Theory and Applications*, Birkhauser, Boston, USA, 1999.
[27] Kanwal, M., Wang, X., Shahzad, H., Chen, Y., Sajid, M., Mathematical modeling of micropolar fluid in blade coating using lubrication theory, *SN Applied Sciences,* **2**, 202, 561.
[28] Shamshuddin, M.D., Sheri, S.R., Anwar Bég, O., Oscillatory dissipative conjugate heat and mass transfer in chemically reacting micropolar flow with wall couple stress: A finite element numerical study, *Proceedings of the Institution of Mechanical Engineers, Part E: Journal of Process Mechanical Engineering,* 233(1), 2019, 48-64.
[29] Sherief, H.H., Faltas, M.S., El-Sapa, S., Interaction between two rigid spheres moving in a micropolar fluid with slip surfaces. *Journal of Molecular Liquids,* 290, 2019, 111165.
[30] Sharma, A., Sharma, R.P., Optimizing shear rate in unsteady stagnation point flow of micro-polar ternary nanofluid flow over a stationary plate: A statistical approach, *ZAMM - Journal of Applied Mathematics and Mechanics,* 105(11), 2025, e70276.
[31] Koh, J.C.Y., Price, J.F., Non-similar boundary-layer heat transfer of a rotating cone in forced flow, *ASME Journal of Heat and Mass Transfer*, 89(2), 1967, 139–145.
[32] Patil, P.M., Benwadi, S., The mixed convection flow of a Williamson nanoliquid over a rotating sphere with the aspects of activation energy, *International Journal of Modelling and Simulation*, 44 (1), 2022, 31-43.
[33] Kumar, D., Sahu, A.K., Forced convection heat transfer from a rotating elliptic cylinder in the laminar flow regime, *Proc. 25th National and 3rd International ISHMT-ASTFE Heat and Mass Transfer Conference (IHMTC-2019)*, IIT Roorkee, Roorkee, India, December 28-31, 2019.
[34] Weidner, D.E., Analysis of the flow of a thin liquid film on the surface of a rotating, curved, axisymmetric substrate, *Physics of Fluids,* 30(8), 2018, 082110.
[35] Lee, A., Brun, P.T., Marthelot, J., Balestra, G., Gallaire, F., Reis, P.M., Fabrication of slender elastic shells by the coating of curved surfaces. *Nature Communications*, 7, 2016, 11155.
[36] Kang, D., Nadim, A., Chugunova, M., Dynamics and equilibria of thin viscous coating films on a rotating sphere, *Journal of Fluid Mechanics*, 791, 2016, 495-518.
[37] Wang, C.Y., Boundary layers on rotating cones, discs and axisymmetric surfaces with a concentrated heat source, *Acta Mechanica*, 81, 1990, 245–251.
[38] Oke, A.S., Mutuku, W.N., Significance of Coriolis force on Eyring-Powell flow over a rotating non-uniform surface, *Applications and Applied Mathematics: An International Journal,* 16 (1), 2021, 643–661.
[39] Mustafa, M., Cattaneo-Christov heat flux model for rotating flow and heat transfer of upper-convected Maxwell fluid, *AIP Advances*, 5, 2015, 047109.
[40] Ibrahim, W., Three-dimensional rotating flow of Powell-Eyring nanofluid with non-Fourier's heat flux and non-Fick's mass flux theory, *Results in Physics*, 8, 2018, 569-577.
[41] Nadeem, S., Saleem, S., Mixed convection flow of Eyring–Powell fluid along a rotating cone, *Results in Physics,* 4, 2014, 54-62.
[42] Zhang, Q., Zhang, B.Y., Guo, B.H., Guo, Z.X., Yu, J., High-temperature polymer conductors with self-assembled conductive pathways, *Composites Part B: Engineering,* 192, 2020, 107989.
[43] Wen, Y.H., Wang, C.C., Cyue, G.S., Kuo, R.H., Hsu, C.H., Chang, R.-Y., Retrieving Equivalent Shear Viscosity for Molten Polymers from 3-D Nonisothermal Capillary Flow Simulation, *Polymers*, 13, 2021, 4094.
[44] Padmaja, K., Rushi Kumar, B., Viscous dissipation and chemical reaction effects on MHD nanofluid flow over a vertical plate in a rotating system, *ZAMM-Journal of Applied Mathematics and Mechanics,* 103(9), 2023, e202200471.
[45] Goud, B.S., Nandeppanavar, M.M., Ohmic heating and chemical reaction effect on MHD flow of micropolar fluid past a stretching surface, *Partial Differential Equations in Applied Mathematics,* 4, 2021, 100104.
[46] Raju, S.S.K., Dynamical dissipative and radiative flow of comparative an irreversibility analysis of micropolar and hybrid nanofluid over a Joule heating inclined channel, *Scientific Reports*, 13, 2023, 5356.
[47] Cullity, B.D., *Introduction to Magnetic Materials,* Addison-Wesley Pub. Co, Reading, 1972.
[48] Anwar Bég, O., Abdul Gaffar, S., Ramachandra Prasad, V., Uddin, M.J., Computational solutions for non-isothermal, nonlinear magnetoconvection in porous media with Hall/ionslip currents and Ohmic dissipation, *Engineering Science and Technology – An International Journal,* 19(1), 2016, 377-394.
[49] Keller H.B., Numerical methods in boundary-layer theory, *Annal Review of Fluid Mechanics*, 10, 1978, 417-433.
[50] Powell, R.E., Eyring, H., Mechanism for relaxation theory of viscosity, *Nature*, 154, 1944, 427–428.
[51] Anwar Bég, O., *Numerical methods for multi-physical magnetohydrodynamics*, Chapter 1, pp. 1-112, New Developments in Hydrodynamics Research, Nova Science, New York, 2012.
[52] Abo-Eldahab, E.M., Elaziz, M.A., Hall current and ohmic heating effects on mixed convection boundary layer flow of a micropolar fluid from a rotating cone with power-law variation in surface temperature, *International Communications in Heat and Mass Transfer*, 31(5), 2004, 751–762.
[53] Thirumalaisamy, K., Sivaraj, R., Prasad, V.R., Anwar Bég, O., Leung, H.H., Kamalov, F., Panneer Selvam, R., Comparative heat transfer analysis of electroconductive water and kerosene hybrid nanofluids in a square porous cavity using the non-Fourier heat flux model, *Physics of Fluids* 34, 2022, 122016.
[54] Kumaran, G., Sivaraj, R., Ramachandra Prasad, V., Anwar Beg, O., Leung, H.H., Kamalov, F., Numerical study of axisymmetric magneto-gyrotactic bioconvection in non-Fourier tangent hyperbolic nano-functional reactive coating flow of a cylindrical body in porous media, *The European Physical Journal Plus,* 136, 2021, 1107.
[55] Ramesh Reddy, P., Abdul Gaffar, S., Anwar Beg, O., Md. Hidayathulla Khan, B., Hall and ion-slip effects on nanofluid transport from a vertical sur face: Buongiorno's model, *ZAMM-Journal of Applied Mathematics and Mechanics/Zeitschrift für Angewandte Mathematik und Mechanik*, 102(3), 2022, e202000 174.

ORCID iD

Shaik Abdul Gaffar https://orcid.org/0000-0002-7368-1658
Osman Anwar Bég https://orcid.org/0000-0001-5925-6711

Sireetorn Kuharat https://orcid.org/0009-0000-5739-9137
Pedakamu Ramesh Reddy https://orcid.org/0000-0002-6666-7444

How to cite this article: Abdul Gaffar S. et al., Magneto-Convection Flow of Micropolar Eyring-Powell Fluid from a Revolving Cone with Hall Current and Ohmic Heating Effects, *J. Appl. Comput. Mech.*, xx(x), 2026, 1–19. https://doi.org/10.22055/jacm.2026.48643.5388